РОССИЙСКИЙ ГОСУДАРСТВЕННЫЙ ПЕДАГОГИЧЕСКИЙ УНИВЕРСИТЕТ им. А. И. ГЕРЦЕНА
HERZEN STATE PEDAGOGICAL UNIVERSITY of RUSSIA

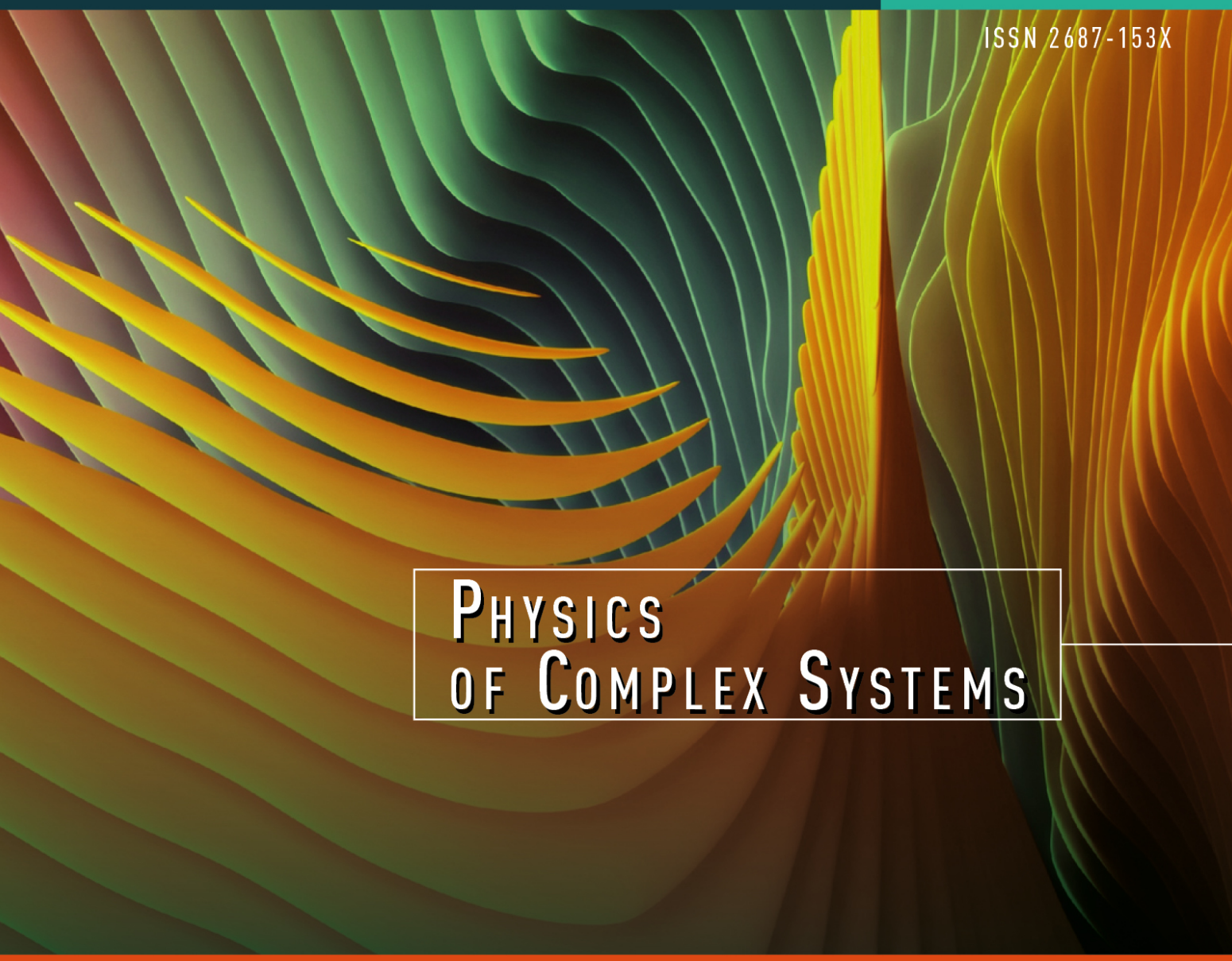

ISSN 2687-153X

Physics of Complex Systems

Т. 3 № 2 2022

Vol. 3 No. 2 2022

Herzen State Pedagogical University of Russia

ISSN 2687-153X (online)
physcomsys.ru
https://www.doi.org/10.33910/2687-153X-2022-3-2
2022. Vol. 3, no. 2

PHYSICS OF COMPLEX SYSTEMS

Mass Media Registration Certificate El No. FS77-77889, issued by Roskomnadzor on 10 February 2020
Peer-reviewed journal
Open Access
Published since 2020
4 issues per year

Publishing house of Herzen State Pedagogical University of Russia
48 Moika Emb., Saint Petersburg 191186, Russia
E-mail: izdat@herzen.spb.ru
Phone: +7 (812) 312-17-41

Data size 7,11 Mbyte
Published at 30.06.2022

Editors of the English text *I. A. Nagovitsyna, A. S. Samarsky*
Cover design by *O. V. Rudneva*
Layout by *A. M. Khodan, L. N. Kliuchanskaya*

CONTENTS

Condensed Matter Physics. Dielectrics

UDC 538.9

EDN EAWOSX

https://www.doi.org/10.33910/2687-153X-2022-3-2-55-59

Molecular mobility research in polyethylene composite films

Yu. A. Gorokhovatskiy[1], E. A. Volgina[1], A. N. Ivanova[1], D. E. Temnov✉[1]

[1] Herzen State Pedagogical University of Russia, 48 Moika Emb., Saint Petersburg 191186, Russia

Authors

Yuriy A. Gorokhovatskiy, ORCID: 0000-0001-5085-2525, e-mail: gorokh-yu@yandex.ru

Elena A. Volgina, e-mail: Volgina.elena.1999@mail.ru

Anna N. Ivanova, e-mail: ivannnik@inbox.ru

Dmitry E. Temnov, ORCID: 0000-0002-9560-4346, e-mail: detem@yandex.ru

For citation: Gorokhovatskiy, Yu. A., Volgina, E. A., Ivanova, A. N., Temnov, D. E. (2022) Molecular mobility research in polyethylene composite films. *Physics of Complex Systems*, 3 (2), 55–59. https://www.doi.org/10.33910/2687-153X-2022-3-2-55-59. EDN EAWOSX.

Received 18 March 2022; reviewed 15 April 2022; accepted 20 April 2022.

Funding: This study is part of the State-Commissioned Assignment of the Ministry of Education of Russia, project No. FSZN-2020-0026.

Abstract. α-relaxation in composite films of low-density polyethylene with soot particles was investigated through thermostimulated depolarisation and differential scanning calorimetry. It is shown that the joint application of these methods can be used to determine the number of relaxers involved in the relaxation processes of a polymer above its glass transition temperature. The parameters and the number of electrically active defects in composite polyethylene films filled with different percentages of technical carbon are calculated.

Keywords: polyethylene composite films, thermal activation spectroscopy, differential scanning calorimetry, relaxation, electrically active defects

Introduction

High-pressure polyethylene (LDPE) plates of 11503-070 (GOST 16337-77) with a density of 0.92 g/cm^3 were used as research objects. The polymer was mixed with the filler on laboratory microrolls at a temperature of 135 ± 5 °C with a mixing time of 3 min. The 0.2 mm thickness plates were prepared according to GOST 12019-66 at a temperature of 170 ± 5 °C with pressure hold time of 5 min.

Technical carbon (soot) was used as a filler. Radiographic investigation of soot particles has shown that they are composed of separate, small-sized, graphite-like crystalline cells. Carbon atom location in the layer is the same as in graphite, while the distance between the layers is greater than in graphite crystals. The locations of the ends of parallel layers on the surface show an increase in energy and, consequently, greater adsorption capacity (Shevchenko 2010).

As shown in (Alekhina et al. 2019; Boriev et al. 2019; Gorokhovatsky et al. 2020), polyethylene films demonstrate multiple relaxations, referred to as α-, β- and γ-in order of decreasing temperature of their observation. There is an α relaxation in the area of 60 °C, which is considered the most complex relaxation and involves at least two mechanisms of molecular mobility. One of them is the beginning of rotational movement inside the crystal, and the other is the sliding of grains' borders between layers, i. e., the shift of chains to half of the primitive cell along the molecular axis (Bharadwaj, Boyd 2001).

In the area −60 °C ÷ −30 °C, β-relaxation is observed in polyethylene, which is associated with glass transition of the polymer. γ-relaxation at a temperature of about −120 °C is usually attributed to

a sufficiently localised molecular motion in the polymer chains (Beatty, Karasz 1979). It should be noted that the intensity of the α transition in polyethylene is usually much lower than the intensity of the transition in the field of glass transition. It was recorded in the temperature range of 10–120 °C, depending on sample preparation and measurement techniques. The temperature T_α, at which the α-transition occurs, correlates with the degree of crystallinity of the sample (Ashcraft, Boyd 1976). However, it was shown that this temperature primarily depends on average crystallite thickness (Alberola et al. 1990; Popli et al. 1984). The dependence of T_α on crystallite thickness is expressed particularly strongly in the range from 50 to 200 °C; with thicknesses exceeding the given one changes in the transition temperature are relatively small (Popli et al. 1984). This relationship is illustrated in Fig. 1.

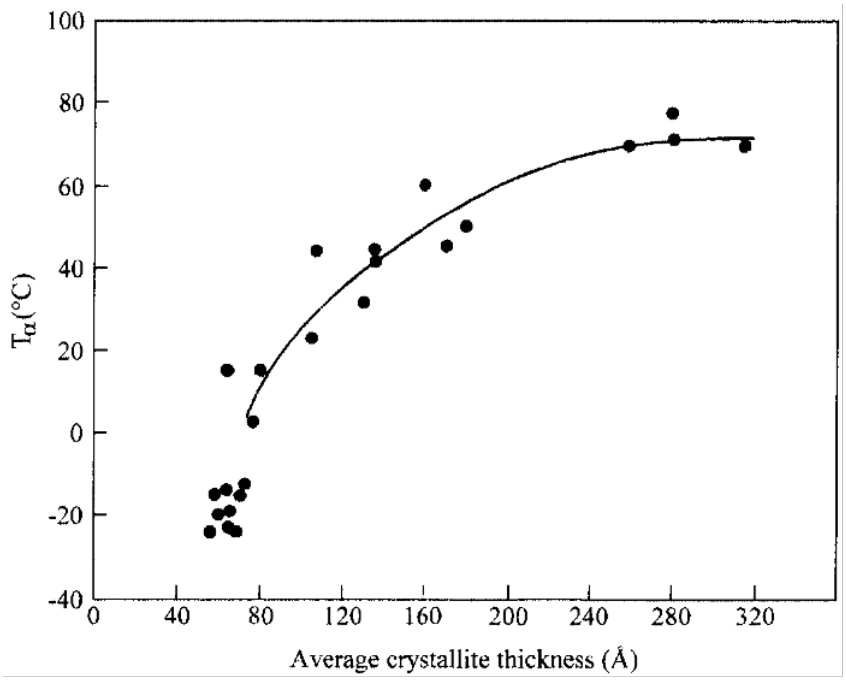

Fig. 1. The dependence of the temperature of α-relaxation in polyethylene from the average crystallite thickness (Popli et al. 1984)

In this paper, α-relaxation in low density polyethylene was investigated with thermostimulated depolarisation and differential scanning calorimetry.

Experimental results and discussion

For the study of electrical relaxation processes in polymeric materials, the methods of thermoactivational current or charge spectroscopy are widely used. This choice is explained by high data yield (high sensitivity and resolution) and ease of technical implementation and experimental data processing.

However, in many cases, e. g., near glass transition temperatures and mechanical relaxations of polymers, the use of traditional methods of experimental results processing for thermal activation spectroscopy leads to abnormally high values of activation energy of E_a electrically active defects (EAD) participating in the relaxation process and unrealistic relaxation time values less than 10^{-20} seconds (Shabanova, Temnov 2021). This is due to the fact that in this case the relaxation process involves the cooperative movement of molecular chain segments, and the precise determination of the activation energy of one relaxer requires taking into account the change in the free volume of the polymer during the relaxation transition.

 https://www.doi.org/10.33910/2687-153X-2022-3-2-55-59

There is an empirical analysis method, based on an equation of activated Eyring states, that is commonly used for such situations and that may give more physically realistic EAD parameters (Bucci et al. 1966). In this case, the following equation in used:

$$\tau(T) = \frac{h}{kT} \exp\left(\frac{\Delta H}{RT}\right) \exp\left(-\frac{\Delta S}{R}\right). \tag{1}$$

where k is Boltzmann's constant, h is Plank's constant, and ΔH, ΔS are the enthalpy of the activated states end the entropy and free energy, respectively. It follows that the construction of a graph corresponding to equation (1) in Arrhenius coordinates $\ln(1/\tau T) \sim 1/T$ makes it possible to calculate the enthalpy and the entropy, and only then the activation energy:

$$E_a = \Delta H - T\Delta S \tag{2}$$

and τ_0. Relaxation times $\tau(T)$ can be obtained from experimental spectra of TSC-TS (method of fractional purification) using the standard Bucci-Fieschi-Guidi method (Bucci et al. 1966).

Figs. 2–3 show the curves of the TSD in the temperature range of α-relaxation obtained for LDPE samples with 5% and 20% of technical carbon obtained with fractional purification (Shabanova, Temnov 2021).

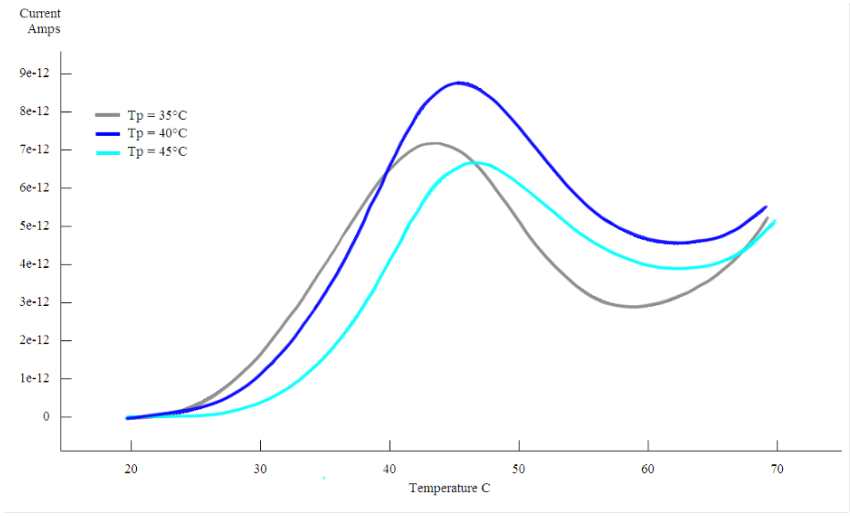

Fig. 2. TSC-TS curves for LDPE samples with 5% technical carbon

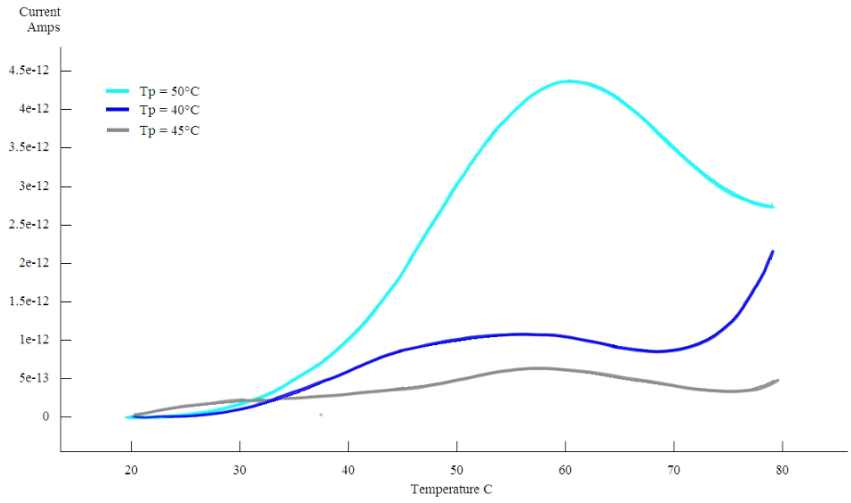

Fig. 3. TSC-TS curves for LDPE samples with 20% technical carbon

The graphs show that as the filler percentage increases, the maximum of the relaxation process shifts to the high temperature area by about 13–15 °C. According to (Popli et al. 1984), this may indicate some increase in the crystallite thickness while increasing the filler concentration.

The activation energy per EAD calculated on the basis of formula (2), taking into account the measurement error, was almost the same and equal to 0.94 ± 0.02 eV. However, the transition enthalpy ΔH for different filler concentrations differs significantly: it was 1.82 eV for 5% filler concentration and 0.87 eV for 20% concentration per relaxer.

Another quite popular method for testing α-transitions in polymers is differential scanning calorimetry. Many researchers investigate phenomena occurring in polymers above the glass transition temperature within the framework of kinetic representations, thermodynamics, fluctuation theory or free volume concept, which are not necessarily mutually exclusive (Berstein, Egorov 1990). With the DSC method, it is possible to determine the glass transition temperature, the width of the glass transition interval, as well as the activation energy of the transitions lying above the glass transition temperature calculated for a mass unit of the polymer.

The comparison of the data obtained for the α-relaxation of polyethylene by TSD and DSC methods makes it possible to determine the number of relaxers involved in this relaxation process.

Fig. 4 shows the DSC heating curves for LDPE samples with different technical carbon content.

In the range of 50–60 °C, a relaxation process is clearly observed, attributed to the α-relaxation of the LDPE. Experimental DSC data processing with dedicated Callisto software makes it possible to determine the change of enthalpy of this transition, indicated in Table 1.

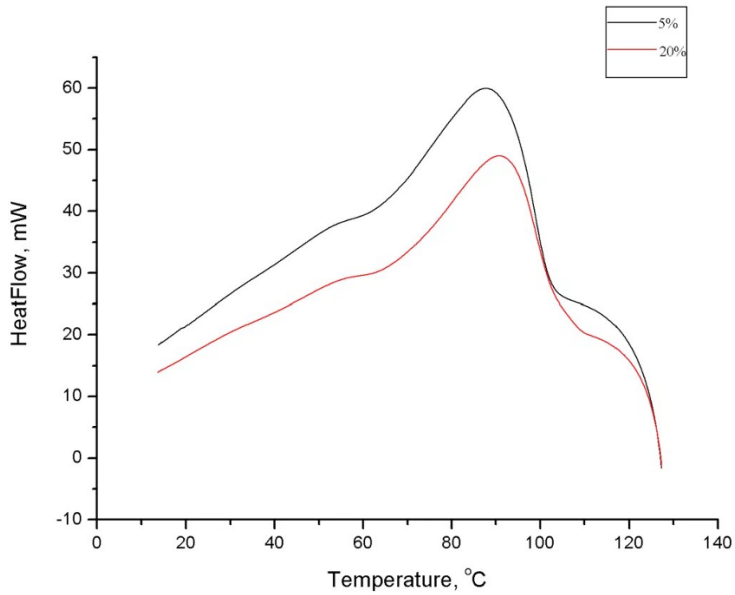

Fig. 4. DSC curves for LDPE samples with 5% and 20% of technical carbon

Table 1. Values of enthalpy changes for PEVD with different technical carbon content

Soot content (%)	Enthalpy change ΔH (J/g)	Number of relaxers (pc/g)
5%	–1.713	5.8 × 1018
20%	–1.601	1.1 × 1019

Taking into account the data obtained with TSD, the number of relaxers involved in relaxation was also determined. As the filler content increases, the number of relaxers increases significantly, which can be explained by the increase in the polymer's degree of crystallinity when the filler is applied and filler particles become the centres of crystallisation of the polymer matrix. Further research by independent methods is needed to accurately interpret the results.

 https://www.doi.org/10.33910/2687-153X-2022-3-2-55-59

Conclusion

The combined use of thermal activation spectroscopy and thermal analysis methods in polymer research makes it possible to obtain additional information on relaxation processes observed above the glass transition temperature. This paper shows that the increase in the filler content in polyethylene affects the parameters of the relaxation process: as the filler content increases, the crystallite thickness increases and the number of kinetic units involved in the relaxation process increases as well.

Conflict of Interest

The authors declare that there is no conflict of interest, either existing or potential.

References

Alberola, N., Cavaille, J. Y., Perez, J. (1990) Mechanical spectrometry of alpha relaxations of high-density polyethylene. *Journal of Polymer Science: Polymer Physics Edition*, 28 (4), 569–586. https://doi.org/10.1002/polb.1990.090280410 (In English)

Alekhina, R. A., Lomovskaya, V. A., Simonov-Emelyanov, I. D. et al. (2019) Relaxation and physicomechanical characteristics of polyethylenes with different molecular weights. *Fine Chemical Technologies*, 14 (6), 104–114. https://doi.org/10.32362/2410-6593-2019-14-6-104-114 (In English)

Ashcraft, C. R., Boyd, R. H. (1976) A dielectric study of molecular relaxation in oxidized and chlorinated polyethylenes. *Journal of Polymer Science: Polymer Physics Edition*, 14 (12), 2153–2193. https://doi.org/10.1002/pol.1976.180141204 (In English)

Beatty, C. L., Karasz, F. E. (1979) The glass transition of linear polyethylene. *Journal of Macromolecular Science. Part C. Polymer Reviews*, 17 (1), 37–60. https://doi.org/10.1080/00222357908080904 (In English)

Berstein, V. A., Egorov, V. M. (1990) *Differentsial'naya skaniruyushchaya kalorimetriya v fizikokhimii polimerov [Differential scanning calorimetry in physicoche of polymers]*. Leningrad: "Khimiya" Publ., 256 p. (In Russian)

Bharadwaj, R. K., Boyd, R. H. (2001) Conformational dynamics in polyethylene under isochoric conditions: A molecular dynamics simulation study. *Journal of Chemical Physics*, 114 (11), 5061–5068. https://doi.org/10.1063/1.1345878 (In English)

Boriev, A. A., Pshikachev, A. G., Thakov, R. B. (2019) Osobennosti dinamicheskikh i mekhanicheskikh svojstv modifitsirovannogo polietilena nizkoj plotnosti [Features of dynamic and mechanical properties of modified low density polyethylene]. *Izvestiya Kabardino-Balkarskogo gosudarstvennogo universiteta — Proceedings of the Kabardino-Balkarian State University*, 9 (4), 34–38. (In Russian)

Bucci, C., Fieschi, R., Guidi, G. (1966) Ionic thermocurrents in dielectrics. *Physical Review*, 148 (2), article 816. https://doi.org/10.1103/PhysRev.148.816 (In English)

Gorokhovatsky, Yu. A., Demidova, N. S., Temnov, D. E. (2020) Electric charge relaxation in the polyethylene with mineral inclusions of diatomite. *St. Petersburg Polytechnic University Journal — Physics and Mathematics*, 13 (2), 9–16. https://doi.org/10.18721/JPM.13201 (In English)

Popli, R., Glotin, M., Mandelkern, L., Benson, R. S. (1984) Dynamic mechanical studies of α and β relaxations of polyethylenes. *Journal of Polymer Science: Polymer Physics Edition*, 22 (3), 407–448. https://doi.org/10.1002/pol.1984.180220306 (In English)

Shabanova, N. S., Temnov, D. E. (2021) Analysis of the TSD spectra of polymers near the glass transition temperature using the fractional purification method. *Physics of Complex Systems*, 2 (4), 157–164. https://doi.org/10.33910/2687-153X-2021-2-4-157-164 (In English)

Shevchenko, V. G. (2010) *Osnovy fiziki polimernykh kompozitsionnykh materialov [Basics of physics of polymer composite materials]*. Moscow: Moscow State University Publ.,98 p. (In Russian)

Condensed Matter Physics. Dielectrics

UDC 537.3

EDN HISZON

https://www.doi.org/10.33910/2687-153X-2022-3-2-60-65

Electrophysical properties of chitosan-based composite films filled with single-wall carbon nanotubes

A. M. Kamalov✉[1], V. V. Kodolova-Chukhontseva[1], E. M. Ivan'kova[2], M. E. Borisova[1], V. E. Yudin[2]

[1] Peter the Great St. Petersburg Polytechnic University, 29 Polytechnicheskaya Str., Saint Petersburg 195251, Russia
[2] Institute of Macromolecular Compounds RAS, 31 Bolshoy Ave., Saint Petersburg 199004, Russia

Authors

Almaz M. Kamalov, ORCID: 0000-0003-2044-957X, e-mail: spb.kamalov@gmail.com

Vera V. Kodolova-Chukhontseva, ORCID: 0000-0001-8314-5317, e-mail: vera_kodolova@mail.ru

Elena M. Ivan'kova, ORCID: 0000-0002-4823-0695, e-mail: ivelen@mail.ru

Margarita E. Borisova, ORCID: 0000-0003-0761-6302, e-mail: vladimirl.borisov@gmail.com

Vladimir E. Yudin, ORCID: 0000-0002-5517-4767, e-mail: yudin@hq.macro.ru

For citation: Kamalov, A. M., Kodolova-Chukhontseva, V. V., Ivan'kova, E. M., Borisova, M. E., Yudin, V. E. (2022) Electrophysical properties of chitosan-based composite films filled with single-wall carbon nanotubes. *Physics of Complex Systems*, 3 (2), 60–65. https://www.doi.org/10.33910/2687-153X-2022-3-2-60-65. EDN HISZON.

Received 21 March 2022; reviewed 15 April 2022; accepted 20 April 2022.

Funding: The study was supported by the Russian Science Foundation, grant No. 19-73-30003.

Abstract. This work focuses on new chitosan-based composite materials. In order to improve chitosan conductivity, single-wall carbon nanotubes (SWCNT) were added as a filler. The structure of the composites was studied using a scanning electron microscope. It is shown that the addition of SWNCT filler leads to chitosan structure ordering. The increase in SWCNT content from 0 wt.% to 3.0 wt.% leads to an increase in composite film conductivity from 10^{-11} to 10 S/m, with the relative dielectric permittivity change from 5.5 to 26 at 1 kHz. The effect of moisture on the films' dielectric properties was also studied.

Keywords: chitosan, nanotube, conductivity, dielectric properties, percolation threshold

Introduction

In recent years, polymer materials have been widely used in cell technology, regenerative medicine, or as a part of devices for open wound treatment. For these materials to be used in such applications, they do not only need an approval for medical use, but should also have suitable properties ensuring their bioactivity. In order to achieve this, the structure of a material needs to be as similar to the structure of a living tissue as possible (Vladkova 2010). One of the most effective cell regulation technologies is the use of electrical stimulation through conducting materials (Liu et al. 2021).

Single wall carbon nanotubes (SWCNT) are a promising filler for composite materials, which can significantly alter the initial electrophysical properties of a polymer film. SWCNT are used as drug carriers (Chen et al. 2008; Cheng et al. 2011; Pan et al. 2009), biosensors and composite matrices in cell technology (Abarrategi et al. 2008; Guo, Ma 2018; Mitrofanova et al. 2014). They have recently been used as a conductive filler in composite materials (Matrenichev et al. 2018) and in stem cell growth projects (Lorite et al. 2019; Lovat et al. 2005).

Chitosan is one of the most promising polimers for medical use in dermal regeneration technologies. Made from chitin, chitosan has a full range of biological properties, such as biocompatibility, bioactivity

and bioresorbability (Kumar 2000). Although chitosan-based materials possess useful medicinal properties, their conductivity is generally insufficient. Electrical signals are involved in various biological processes, such as cell communication and tissue regeneration. Therefore, tissue engineering matrices need a certain level of electrical conductivity to increase their biocompatibility, stimulate cell processes and facilitate cell adhesion, proliferation and differentiation (Stewart et al. 2015; Yang et al. 2016).

The addition of SWCNT (up to 10 m%) leads to an increase in the conductivity of a material and improves its mechanical properties (Huang 2020; Matrenichev et al. 2018). A low concentration of SWCNT makes it possible to minimise potential polymer cytotoxicity.

The goal of this work was to develop new conductive chitosan-based composites and to study the effect of SWCNT addition on the composites' electrophysical properties.

Materials and methods

The composite films were obtained from the mixture of SWCNT and 4% solution of chitosan in 2% acetic acid. The samples were made from shrimp chitosan (CS) manufactured by Biolog Heppe GmbH (Germany) with a molecular mass of $1.64 \times 10^5 – 2 \times 10^5$ and deacetylation degree of 92.4%. Single wall carbon nanotubes were purchased from Carbon Chg, Russia. The average diameter of SWCNT was equal to 1.4 ± 0.3 nm; their length was 1–5 μm. An aqueous dispersion containing SWCNT was subjected to ultrasound treatment using an IL10–0.63 ultrasonic bath for 15 min (25 kHz, 630 W). Chitosan was introduced into the SWCNT aqueous dispersion in the amount resulting in polymer concentration of 4.0% and the required chitosan/SWCNT ratio.

The mixture of chitosan and SWCNT in water was stirred for 30 min in order to achieve chitosan swelling and partial dissolving. After that, acetic acid was added to the mixture (2% concentration). The solution was stirred for 180 min, filtered and deaerated in a vacuum chamber for 24 h at a pressure of 10 kPa. SWCNT contents were 0.1, 0.5, 1.0 and 3.0 wt.%. The films were prepared by extruding the solution onto glass substrate through a slit die. Subsequently, the films were dried at 50 °C for 1 h. The films on a glass substrate were deaerated in a vacuum chamber at 10 kPa and dried in air at room temperature (24 h each). The obtained films were exposed to 10% aqueous solution containing NaOH and C2H5OH (1:1) for 10 min, then they were washed with distilled water and dried in air (Fig. 1). The film thickness was 30 ± 5 μm.

Fig. 1. Optical images of chitosan-based films containing 0.0.5, and 3 wt.% of SWCNT (a, b, c, respectively)

The structure of nanocomposite chitosan films was studied with electron microscopy, using SUPRA-55VP instrument (Carl Zeiss, Germany).

The electrical conductivity of the samples was measured under isothermal conditions at 25 °C using a Keithley 6487 picoammeter (both two-electrode and four-electrode schemes were used).

The dielectric spectra were obtained using a "Concept 22" broadband dielectric spectrometer (Novocontrol Technologies) equipped with an ALPHA-ANB high-resolution automatic frequency analyser. Dielectric permittivity and dielectric loss were measured in the frequency range of $1–10^6$ Hz; the input signal amplitude was 1 V. Before measurements, platinum electrodes 10 nm thick were placed onto the samples.

Results and discussion

The structure of the initial chitosan and the composites was studied using a SEM. SEM images of the chitosan film and the SWCNT-containing composite films are shown in Fig. 2. The structure of a chito-

san film (Fig. 2) contains lamellar elements, matching the data given in (Dobrovolskaya et al. 2018; Dresvyanina et al. 2020). The film containing 0.5 wt.% of SWCNT (Fig. 2) has a denser and more homogeneous structure.

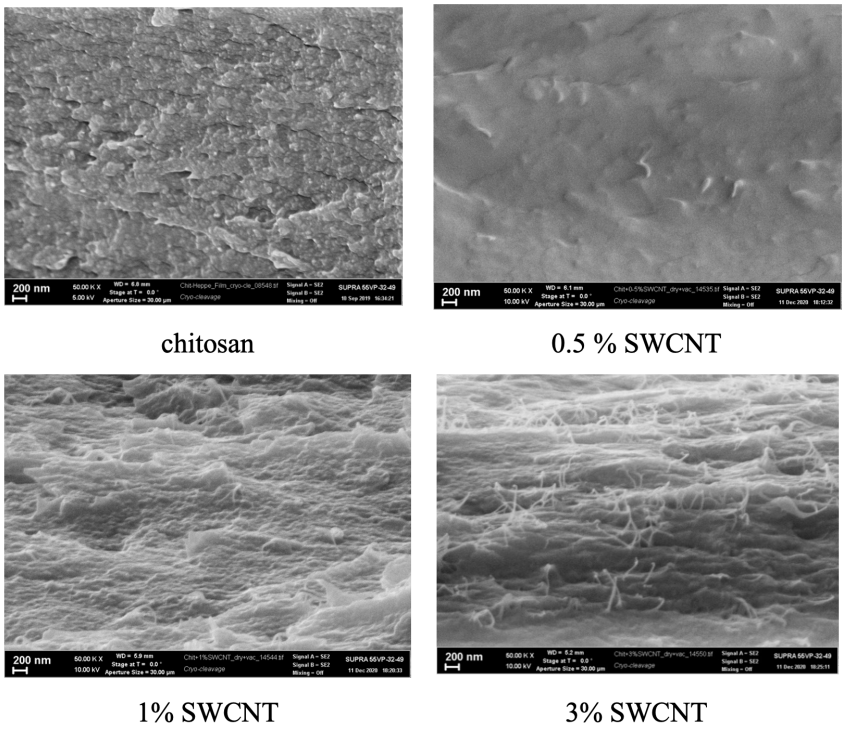

Fig. 2. SEM images of the chitosan film and the SWCNT-containing composite films

When the content of SWCNT in the composite reaches 1.0%, individual carbon nanotubes can be seen on the fracture surface (Fig. 2). The amount of nanotubes on fracture surface increases in the sample with 3% SWCNT (Fig. 2). This conducting filler structure should result in high conductivity of the composite material.

Fig. 3 shows that the increase in SWCNT content from 0.5 wt.% to 1.0 wt.% leads to an increase in the conductivity of the composite film (from 10^{-6} to 10^{-2} S/m). A sharp increase in the conductivity of the material with a slight change in the content of the filler indicates the formation of the conductivity percolation threshold.

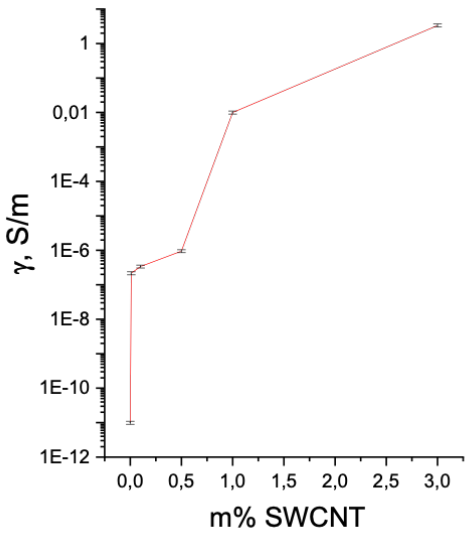

Fig. 3. The volume conductivity of chitosan-based composite films versus SWCNT mass percentage

https://www.doi.org/10.33910/2687-153X-2022-3-2-60-65

The further increase in filler mass concentration (up to 3 m%) leads to a significantly slower increase in sample conductivity due to the formation of a grid-like SWCNT structure in the bulk of chitosan.

Fig. 4 shows frequency dependences of $\varepsilon''(f)$ of the composite samples.

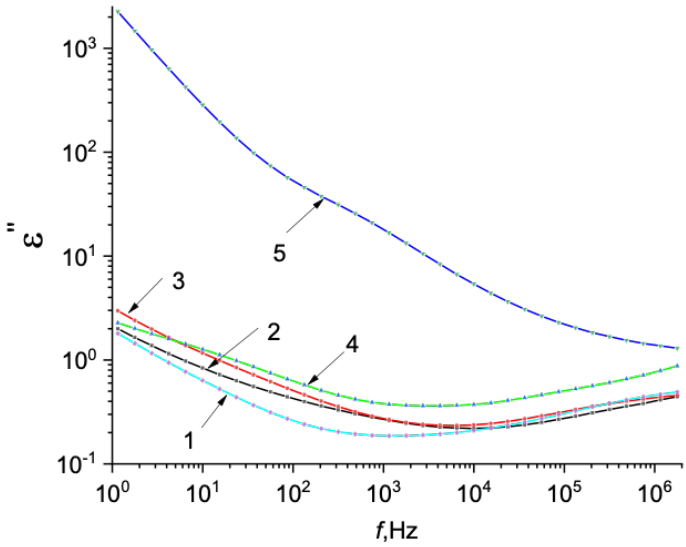

Fig. 4. Frequency dependences of the $\varepsilon''(f)$ of the composite samples (SWCNT m% 0 (1), 0.01 (2), 0.1 (3), 0.5 (4) and 1.0 (5))

The plot suggests that the initial chitosan films have the lowest dielectric loss value (0.03 at 1 kHz). With the increase in the SWCNT concentration, dielectric loss increases to 0.68. The dielectric loss of the sample with 1% SWCNT is much higher due to the increase in the sample's conductivity. The maximum value of dielectric loss is probably tied to Maxwell—Wagner—Sillars (MWS) polarisation (Maxwell 1873). The surface boundary between SWCNT and chitosan can be described as multiple nanocapacitors, their stored charge is determined by the difference between the conductivities of SWCNT and chitosan (Xia et al. 2017).

Fig. 5 shows that with an increase in SWCNT concentration from 0 m% to 5 m%, composite relative dielectric permittivity increases from 4.4 to 5.7 at 1 MHz. The results achieved are in line with the study (Bonardd, Robles, Barandiaran et al. 2018), where ε' ranges from 6.5 to 5.5 in the frequency range from 1 kHz to 1 MHz.

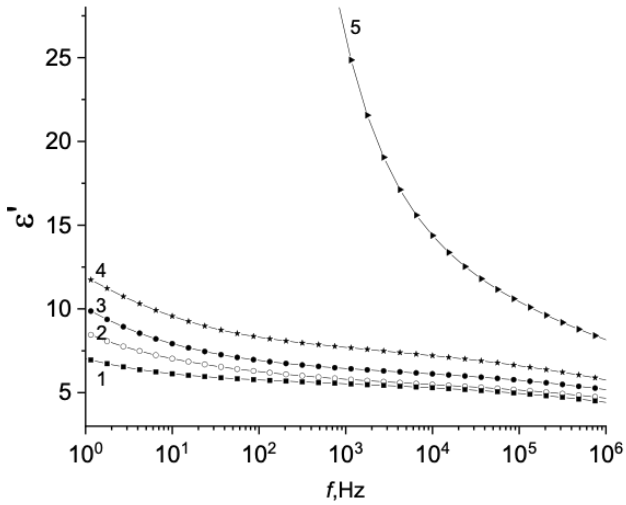

Fig. 5. Frequency dependences of the relative dielectric permittivity of composite samples (SWCNT m% 0 (1), 0.01 (2), 0.1 (3), 0.5 (4) and 1.0 (5))

The inscrease in SWCNT mass concentration up to 1 %m leads to a notable increase in relative dielectric permittivity in the low-frequency range; with the increase of the frequency the relative permittivity decreases.

It is a known fact that chitosan films have high hygroscopic properties, which can affect their relative dielectric permittivity. Fig. 6 shows the dependences between relative permittivity and filler mass percentage. These dependences were achieved at 80 °C, but the drying times were different for curves 2–3.

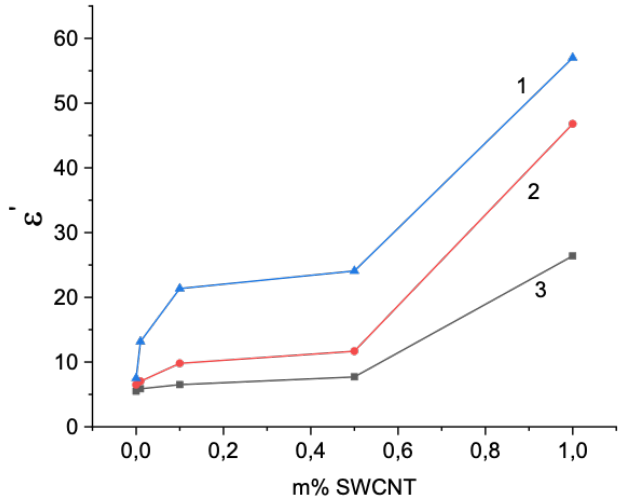

Fig. 6. The relative permittivity versus filler mass percentage at 1 kHz (Drying times: 0 hours (1), 1.5 hours (2) and 3 hours (3))

The plot suggests that the relative permittivity of dried films is lower, this difference is due to water sorption in films that have not been dried.

Conclusion

Biocompatible composite chitosan films with single-walled carbon nanotubes have been obtained. The dependences between their electrophysical properties and nanotube concentrations have been established.

SWCNT insertion promotes chitosan structure ordering and the formation of a denser macromolecule packing. It is shown that with an increase in SWCNT content from 0 to 3 wt.%, electrical conductivity changes from 10^{-11} to 10 S/m. The conductivity percolation threshold is in the range of 0.5–1 wt.%.

It is established that a sharp increase in dielectric losses is observed with an increase in SWCNT concentration above 0.5% by weight. The increase in dielectric losses and permitivity in the low frequency region is due to MVS polarisation. The results obtained make it possible to expand the potential applications of this biocompatible electrically conductive material in tissue engineering.

Conflict of interest

The authors declare that there is no conflict of interest, either existing or potential.

Author contributions

Almaz M. Kamalov and Margarita E. Borisova were involved in conceptualising and conducting the study, writing the original draft and project management. Vera V. Kodolova-Chukhontseva, Elena M. Ivan'kova and Vladimir V. Yudin were involved in conducting the study and reviewing and editing the article.

https://www.doi.org/10.33910/2687-153X-2022-3-2-60-65

References

Abarrategi, A., Gutiérrez, M. C., Moreno-Vicente, C. et al. (2008) Multiwall carbon nanotube scaffolds for tissue engineering purposes. *Biomaterials*, 29 (1), 94–102. https://doi.org/10.1016/j.biomaterials.2007.09.021 (In English)

Bonardd, S., Robles, E., Barandiaran, I. et al. (2018) Biocomposites with increased dielectric constant based on chitosan and nitrile-modified cellulose nanocrystals. *Carbohydrate Polymers*, 199, 20–30. https://doi.org/10.1016/j.carbpol.2018.06.088 (In English)

Chen, J., Chen, S., Zhao, X. et al. (2008) Functionalized single-walled carbon nanotubes as rationally designed vehicles for tumor-targeted drug delivery. *Journal of the American Chemical Society*, 130 (49), 16778–16785. https://doi.org/10.1021/ja805570f (In English)

Cheng, J., Meziani, M. J., Sun, Y. P. et al. (2011) Poly(ethylene glycol)-conjugated multi-walled carbon nanotubes as an efficient drug carrier for overcoming multidrug resistance. *Toxicology and Applied Pharmacology*, 250 (2), 184–193. https://doi.org/10.1016/j.taap.2010.10.012 (In English)

Dobrovolskaya, I. P., Yudin, V. E., Popryadukhin, P. V. et al. (2018) Effect of chitin nanofibrils on electrospinning of chitosan-based composite nanofibers. *Carbohydrate Polymers*, 194, 260–266. https://doi.org/10.1016/j.carbpol.2018.03.074 (In English)

Dresvyanina, E. N., Grebennikov, S. F., Dobrovol'skaya, I. P. et al. (2020) Effect of chitin nanofibrils on the sorption behavior of chitosan-based composite films. *Polymer Science. Series A. Polymer Physics*, 62 (3), 205–212. https://doi.org/10.1134/S0965545X20030050 (In English)

Guo, B., Ma, P. X. (2018) Conducting polymers for tissue engineering. *Biomacromolecules*, 19 (6), 1764–1782. https://doi.org/10.1021/acs.biomac.8b00276 (In English)

Huang, B. (2020) Carbon nanotubes and their polymeric composites: The applications in tissue engineering. *Biomanufacturing Reviews*, 5 (1), article 3. https://doi.org/10.1007/s40898-020-00009-x (In English)

Kumar, M. N. R. (2000) A review of chitin and chitosan applications. *Reactive and Functional Polymers*, 46 (1), 1–27. https://doi.org/10.1016/S1381-5148(00)00038-9 (In English)

Liu, Z., Wan, X., Wang, Z. L. et al. (2021) Electroactive biomaterials and systems for cell fate determination and tissue regeneration: Design and applications. *Advanced Materials*, 33 (32), article 2007429. https://doi.org/10.1002/adma.202007429 (In English)

Lorite, G. S., Ylä-Outinen, L., Janssen, L. et al. (2019) Carbon nanotube micropillars trigger guided growth of complex human neural stem cells networks. *Nano Research*, 12, 2894–2899. https://doi.org/10.1007/s12274-019-2533-2 (In English)

Lovat, V., Pantarotto, D., Lagostena, L. et al. (2005) Carbon nanotube substrates boost neuronal electrical signaling. *Nano Letters*, 5 (6), 1107–1110. https://doi.org/10.1021/nl050637m (In English)

Matrenichev, V. V., Popryadukhin, P. V., Kryukov, A. E. et al. (2018) Properties of film materials based on composite nanofibers from aliphatic copolyamide and carbon nanotubes for tissue engineering. *Polymer Science. Series A. Polymer Physics*, 60, 215–221. https://doi.org/10.1134/S0965545X18020104 (In English)

Maxwell, J. C. (1873) *A treatise on electricity and magnetism*. Oxford: Clarendon Press, 500 p. (In English)

Mitrofanova, I. V., Milto, I. V., Suhodolo, I. V. et al. (2014) Vozmozhnosti biomeditsinskogo primeneniya uglerodnykh nanotrubok [Opportunities of biomedical use of carbon nanotubes]. *Byulleten' sibirskoj meditsiny — Bulletin of Siberian Medicine*, 13 (1), 135–144. https://doi.org/10.20538/1682-0363-2014-1-135-144 (In Russian)

Pan, B., Cui, D., Xu, P. et al. (2009) Synthesis and characterization of polyamidoamine dendrimer-coated multi-walled carbon nanotubes and their application in gene delivery systems. *Nanotechnology*, 20 (12), article 125101. https://doi.org/10.1088/0957-4484/20/12/125101 (In English)

Stewart, E., Kobayashi, N. R., Higgins, M. J. et al. (2015) Electrical stimulation using conductive polymer polypyrrole promotes differentiation of human neural stem cells: A biocompatible platform for translational neural tissue engineering. *Tissue Engineering. Part C: Methods*, 21 (4), 385–393. https://doi.org/10.1089/ten.tec.2014.0338 (In English)

Vladkova, T. G. (2010) Surface engineered polymeric biomaterials with improved biocontact properties. *International Journal of Polymer Science*, 2010, article 296094. https://doi.org/10.1155/2010/296094 (In English)

Xia, X., Zhong, Z., Weng, G. J. (2017) Maxwell–Wagner–Sillars mechanism in the frequency dependence of electrical conductivity and dielectric permittivity of graphene-polymer nanocomposites. *Mechanics of Materials*, 109, 42–50. https://doi.org/10.1016/j.mechmat.2017.03.014 (In English)

Yang, J., Choe, G., Yang, S. et al. (2016) Polypyrrole-incorporated conductive hyaluronic acid hydrogels. *Biomaterials Research*, 20 (1), article 31. https://doi.org/10.1186/s40824-016-0078-y (In English)

Theoretical Physics. Theory of condensed matter

UDC 535

EDN KDLQJF

https://www.doi.org/10.33910/2687-153X-2022-3-2-66-74

Analytical regularities of inversionless superradiance

A. S. Gorbacheva[1], I. V. Ryzhov✉[1]

[1] Herzen State Pedagogical University of Russia, 48 Moika Emb., Saint Petersburg 191186, Russia

Authors

Alisa S. Gorbacheva, e-mail: alisa.gorbacheva@bk.ru

Igor V. Ryzhov, e-mail: igoryzhov@yandex.ru

For citation: Gorbacheva, A. S., Ryzhov, I. V. (2022) Analytical regularities of inversionless superradiance. *Physics of Complex Systems*, 3 (2), 66–74. https://www.doi.org/10.33910/2687-153X-2022-3-2-66-74. EDN KDLQJF.

Received 25 February 2022; reviewed 28 March 2022; accepted 28 March 2022.

Funding: The study did not receive any external funding.

Abstract. The article reports the results of a theoretical study of superradiance of three-level optical systems with a doublet in the ground state (Λ-scheme) placed in a high-quality cavity. Hyperbolic chaos and unpredictable dynamic movements of the system appear on the surface of a multidimensional torus without dissipative losses in the conditions of superradiance without population inversion. The study resulted in the development of conservation laws to reduce the dimension of the phase space. An analytical result is obtained for the special case of a degenerate doublet.

Keywords: superradiance, superradiance without inversion, Λ-scheme, the Duffing equation

Introduction

It is well-known that the necessary condition for Dicke superradiance (SR) (Dicke 1954) is the presence of the initial population inversion of transitions levels (Andreev et al. 1980; 1993; Benedict et al. 1996; Bonifacio et al. 1971; Bonifacio, Lugiato 1975; Gross, Haroche 1982; Kalachev, Samartsev 2003; MacGillivray, Feld 1976; 1981; Rehler, Eberly 1971; Sokolov, Trifonov 1974; Zheleznyakov et al. 1989). Considering our case with three-level Λ-emitters, this restriction is not mandatory. Superradiance is possible even when the initial upper-level population is less than the total population of the lower doublet—SR without population inversion (Carlson et al. 1980; Harris 1989; Kocharovskaya 1997; Kocharovskaya, Khanin 1988; Kocharovskaya, Mandel 1990; Malikov, Trifonov 1984; Malyshev et al. 1998; 2000; 2003; Ryzhov et al. 2012; 2017; Scully 1992; Yuan, Svidzinsky 2012; Zaitsev et al. 1999). The essence of the effect is as follows. If one prepares the initial state of the lower doublet as a coherent superposition, transition to which from the upper state is forbidden, then the orthogonal to the initial superposition, transition to which is allowed, appears to be unpopulated. In this case, the transition from the upper level to this superposition state appears to be inverted at an arbitrarily small population of the upper level. The initial coherent state of the doublet can be created by a short low-frequency π/2-pulse (Malyshev et al. 1998; 2003; Ryzhov et al. 2012; 2017; Zaitsev et al. 1999). Crystals activated by rare earth ions, such as LaF_3:Pr^{3+}, Y_2SiO_5:Pr_{3+}, Y_2SiO_5:Eu^{3+}, Y_2SiO_5:Er^{3+}, etc., are real objects where the conditions for observing SR regimes without inversion can be achieved. At cryogenic temperatures, the conditions of the 4f orbitals of these ions are characterized by a high degree of optical coherence, less than kHz, and very low heterogeneous expansion from MHz to GHz (Ryzhov, Vasil'ev, Kosova et al. 2017). An additional level close to the ground one is a solution to the problem in question.

The article focuses on analytical regularities of the nonlinear dynamics of superradiance of an ensemble of three-level Λ-atoms which are spatially homogeneously and isotropically distributed in a high-Q cyclic cavity. The model of SR proposed in this work is conservative. There are no relaxation losses of SR. The time dynamics of the model is considered in terms of the semiclassical approach:

the ensemble of three-level emitters is described by equations for the density matrix ρ_{mn} (m, n = 1, 2, 3), while the electromagnetic field is described by Maxwell's equations. The conservation of the system results in integrals of motion that considerably reduce the dimension of the phase space of the examined model: ($R^{11} \to R^5$). For the degenerate doublet, we found mapping that reduces the problem of the three-level SR to a nonlinear oscillator with cubic nonlinearity ($R^5 \to R^2$).

Model and formalism

We consider an ensemble of three-level atoms with the Λ-scheme of operation transitions. The atoms are homogeneously distributed along one of the arms of a high-Q cyclic cavity (Fig. 1).

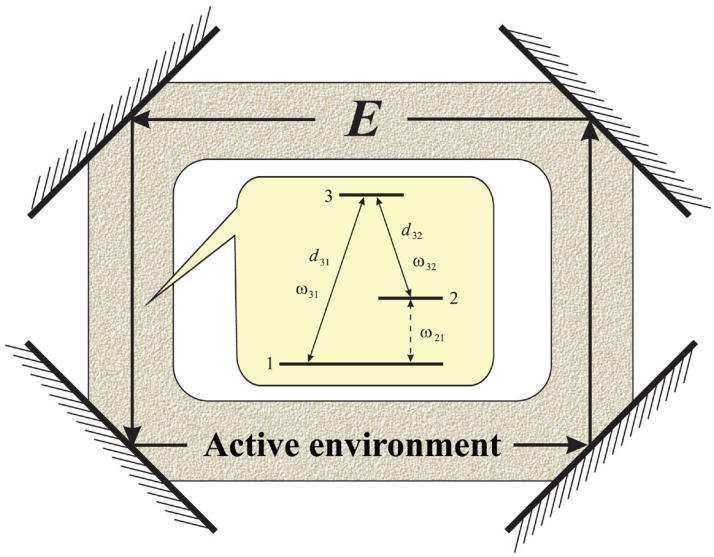

Fig. 1. A diagram of a unidirectional ring cavity. The active medium of Λ-emitters is gray. An inserted picture shows energy-level diagram of Λ-emitters. The number of the level (n = 1,2,3) corresponds to the state of the emitter with energy E_n. Solid and dashed arrows indicate, respectively, the allowed and forbidden transitions between the energy levels of the emitter, with the frequencies of the corresponding transitions ω_{21}, ω_{31}, and ω_{32}, and the transition dipole moments d_{31} and d_{32} ($d_{21} = 0$).

In addition, all vectors (transition dipole moments and polarization of the field) are assumed to be directed identically and perpendicularly to the axis of the system. The evolution of the system then obeys the following (one-dimensional) system of Maxwell—Bloch equations:

$$
\begin{aligned}
\dot{\rho}_{11} &= i\frac{d_{31}E}{\hbar}\left(\rho_{31}-\rho_{13}\right),\\
\dot{\rho}_{22} &= i\frac{d_{32}E}{\hbar}\left(\rho_{32}-\rho_{23}\right),\\
\dot{\rho}_{33} &= -i\frac{d_{31}E}{\hbar}\left(\rho_{31}-\rho_{13}\right)-i\frac{d_{32}E}{\hbar}\left(\rho_{32}-\rho_{23}\right),\\
\dot{\rho}_{21} &= -i\omega_{21}\rho_{21}-i\frac{d_{31}E}{\hbar}\rho_{23}+i\frac{d_{32}E}{\hbar}\rho_{31},\\
\dot{\rho}_{31} &= -i\omega_{31}\rho_{31}-i\frac{d_{31}E}{\hbar}\left(\rho_{33}-\rho_{11}\right)+i\frac{d_{32}E}{\hbar}\rho_{21},\\
\dot{\rho}_{32} &= -i\omega_{32}\rho_{32}-i\frac{d_{32}E}{\hbar}\left(\rho_{33}-\rho_{22}\right)+i\frac{d_{31}E}{\hbar}\rho_{12},\\
\left(\frac{\partial^2}{\partial x^2}-\frac{1}{c}\frac{\partial^2}{\partial t^2}\right)E &= \frac{4\pi}{c^2}\frac{\partial^2 P}{\partial t^2},
\end{aligned}
\qquad (1)
$$

where, ρ_{nm} are the elements of the density matrix of the three-level atom at the point with coordinate x at moment of time t (m, n = 123); d_{31} and d_{32} are the dipole moments of the corresponding transitions, which, without loss of generality, can be considered to be real-valued and positive; ω_{31} and ω_{31} are the frequencies of optical transitions between the upper level 3 and the doublet sublevels 1 and 2; ω_{21} is the frequency of the transition between the sublevels of the doublet; P = N ($d_{31}\rho_{31} + d_{32}\rho_{32} + c.c.$) is the polarization of the medium; N is the concentration of atoms; c is the speed of light in vacuum; E is the electric field strength.

The relaxation of the populations and polarization (homogeneous and related to inhomogeneous broadening) is not taken into account: we assume that the SR time is considerably shorter than all relaxation times and consider the dynamics of superradiance on this scale. In addition, we neglect the decay of the field due to cavity losses. Frequency ω_{21} of the doublet splitting is assumed to be much smaller than frequencies ω_{31} and ω_{32} of the optical transitions. We also assume that the spectrum of SR and the value of doublet splitting ω_{21} do not exceed the spacing between cavity modes, i. e., we restrict ourselves to the single-mode approximation.

We will seek the solution to the system of equations (1) in the form

$$\begin{aligned} \rho_{31} &= R_{31}e^{-i(\omega t-kx)}, \\ \rho_{32} &= R_{32}e^{-i(\omega t-kx)}, \\ E &= Ae^{-i(\omega t-kx)} + c.c, \end{aligned} \tag{2}$$

where $k = \omega/c$, while the field amplitude A and off-diagonal elements R_{31} and R_{32} of the density matrix (in what follows, they will be referred to as the high-frequency coherences) are functions that very slowly change on a scale of the optical period $2\pi/\omega$ and the radiation wavelength $\lambda = 2\pi/k$ — the approximation of slowly varying amplitudes (SVA). Note that an analogous assumption with respect to low-frequency coherence ρ_{21} (on a scale of $2\pi/\omega$) is not used. It is natural to assume that passage time L/c (L is the cavity length) is much shorter than characteristic times of the problem, i. e., during one round trip of the light in the cavity, the state of the medium changes insignificantly. In this case, the retardation can be neglected. Then the field at the input into the active medium (by virtue of a high-quality factor of the cavity) is equal to the field at its output, which also justifies the use of the mean-field approximation. And, finally, let us assume that the $|3\rangle \leftrightarrow |1\rangle$ and $|3\rangle \leftrightarrow |2\rangle$ transition dipole moments are identical ($d_{31} = d_{32} = d$). This is the approximation that is not principal for the problem under consideration.

Taking a standard path from the system of equations (1) to a similar system for SVA, we obtain

$$\dot{\rho}_{11} = ER_{31}^{*} + E^{*}R_{31}, \quad \dot{\rho}_{22} = ER_{32}^{*} + E^{*}R_{32}, \tag{3a}$$

$$\dot{\rho}_{33} = -\left(ER_{31}^{*} + E^{*}R_{31}\right) - \left(ER_{32}^{*} + E^{*}R_{32}\right), \tag{3b}$$

$$\dot{\rho}_{21} = -i\delta\dot{\rho}_{21} + ER_{32}^{*} + E^{*}R_{31}, \tag{3c}$$

$$\dot{R}_{31} = -\frac{i\delta}{2}R_{31} + E\left(\rho_{33} - \rho_{11} - \rho_{21}\right), \tag{3d}$$

$$\dot{R}_{32} = \frac{i\delta}{2}R_{32} + E\left(\rho_{33} - \rho_{22} - \rho_{21}^{*}\right), \tag{3e}$$

$$\dot{E} = R_{31} + R_{32} \tag{3f}$$

here, dots denote the derivatives with respect to the dimensionless time $\tau = t\Omega$, where $\Omega^{-1} = \sqrt{\hbar\left(2\pi\omega d^{2}N\right)^{-1}}$ is the constant that determines the time scale (Ω^{-1}); $\delta = \omega^{21}/\Omega$ is the dimensionless splitting frequency of the doublet; and $E = -idA/(\hbar\Omega)$ is the dimensionless amplitude of the electric field strength. For simplicity, eigenfrequency $\omega = (\omega_{31} + \omega_{32})/2$ of the cavity is considered to be centered between frequencies ω_{31} and ω_{32}.

This system of equations has the following integrals of motion:

$$|E|^{2} + \rho_{33} = \text{const}, \tag{4a}$$

 https://www.doi.org/10.33910/2687-153X-2022-3-2-66-74

$$\rho_{11}-\rho_{22}-\rho_{33}=1, \tag{4b}$$

$$\rho_{11}^2+\rho_{22}^2+\rho_{33}^2+2\left(\left|\rho_{21}\right|^2+\left|R_{31}\right|^2+\left|R_{32}\right|^2\right)=\text{const}, \tag{4c}$$

(4a) shows the law of conservation of the excitation energy of the system, (4b) and (4c) represent the normalization conditions for the density matrix and its square respectively. The presence of integrals of motion makes it possible to considerably simplify the analysis of the dynamics of the three-level SR.

Initial conditions, symmetry, and simplification of the model

The presence of a doublet in the ground state introduces new effects into the response of the system. They are generated by the competition between the transitions $|3\rangle \leftrightarrow |1\rangle$. In connection with this, to investigate the kinetics of the three-level SR, we will choose such initial conditions that will ensure most effective interaction between the parts of the system "cavity + atoms + field", i. e., at any initial population of the upper state and with a minimal delay of the SR pulse. In this regard, let us focus on equations (3d) and (3e) for the high-frequency coherences R_{31} and R_{32}. They contain terms that are proportional to low-frequency coherence ρ_{21}. In this case, if $\rho_{21}(0) \neq 0$, the evolution of initial fluctuations of R_{31} will depend on phase $\rho_{21}(0)$. At positive values of $\rho_{21}(0)$ these fluctuations will decrease; however, if the values of $\rho_{21}(0)$ are negative, these fluctuations, on the contrary, will increase avalanche-like, leading to superradiance. Notably, this possibility arises at any difference of the populations in channels $3 \leftrightarrow 1$ and $3 \leftrightarrow 2$ due to the transformation of the low-frequency coherence $\rho_{21}(0)$ into high-frequency coherences R_{31} and R_{32}. The latter effect is explicitly reflected in the integral of motion (4c). The analysis of superradiance of this Λ-system is significantly simplified upon passage to a new basis $|3\rangle$, $|+\rangle=\left(|1\rangle+|2\rangle\right)/\sqrt{2}$, $|-\rangle=\left(|1\rangle-|2\rangle\right)/\sqrt{2}$, (Malyshev et al. 1998; Ryzhov et al. 2012; 2017; Zaitsev et al. 1999). In this case, the elements of the density matrix are transformed in accordance with the following relations:

$$\begin{aligned}
\rho_{++}&=\frac{1}{2}\left(\rho_{11}+\rho_{22}+2Re\left[\rho_{21}\right]\right),\\
\rho_{--}&=\frac{1}{2}\left(\rho_{11}+\rho_{22}-2Re\left[\rho_{21}\right]\right),\\
\rho_{+-}&=\frac{1}{2}\left(\rho_{11}-\rho_{22}+\rho_{21}-\rho_{21}^{*}\right),\\
R_{3+}&=\frac{1}{\sqrt{2}}\left(R_{31}+R_{32}\right), \quad R_{3-}=\frac{1}{\sqrt{2}}\left(R_{31}-R_{32}\right),
\end{aligned} \tag{5}$$

where ρ_{++} and ρ_{--} are the populations of the active and passive states respectively; ρ_{++} is the low-frequency coherence; and R_{32} and R_{32} are the high-frequency coherences of the corresponding optical channels.

It can be seen from the expression for population ρ_{++} of the active state presented in the relations (5) that for the three-level SR to take place, the presence of an inversion population in active channel $|3\rangle \leftrightarrow |+\rangle$ is necessary, i. e., at the initial moment of time, inequality $\rho_{33}(0) > \rho_{++}(0)$ should be implement. In the ideal case, in which the population of the active state is zero, $\rho_{++}(0) = \rho_{11}(0) + \rho_{22}(0) + 2\mathrm{Re}[\rho^{21}(0)] = 0$, the following conditions should be met:

$$\begin{aligned}
Re\left[\rho_{21}(0)\right]&=\left((\alpha-1)\right)/2, \quad \mathrm{Im}\left[\rho_{21}(0)\right]=0,\\
-Re\left[\rho_{21}(0)\right]&=\rho_{11}(0)+\rho_{22}(0),
\end{aligned} \tag{6}$$

where $\rho_{22}(0) = \alpha$ and $0 < \alpha \leq 1$. In what follows, we will assume that the lower doublet is prepared in a maximally coherent state if conditions (6) are met at the initial moment of time. We emphasize again that, under these starting conditions, superradiance can occur at any initial population $\rho_{33}(0)$ of the upper state, even if there is no inversion population on the whole, when the total initial population of the lower doublet exceeds the initial population of the upper level, $\rho_{11}(0) + \rho_{22}(0) > \rho_{33}(0)$.

If the initial electric field strength is zero,

$$Re\left[E\left(0\right)\right]=Im\left[E\left(0\right)\right]=0 \tag{7}$$

for superradiance to arise, it suffices to set small seed values of the high-frequency coherences, e. g.:

$$Re\left[R_{31}\left(0\right)\right]=Re\left[R_{32}\left(0\right)\right]=\pm R_0, \tag{8}$$

where, without loss of generality, it is assumed that Im [R_{31} (0)] = Im [R_{32} (0)] = 0, while the value of $R_0 \ll 1$. We are not interested in the fluctuations of SR; therefore, initial values R_{31} (0) and R_{32} (0) are specified as determinate parameters, which corresponds to the conditions of the induced SR (Carlson et al. 1980; Malikov, Trifonov 1984).

The system of differential equations (3) with initial conditions (6)–(8) was solved numerically. The following two controlling parameters varied: the initial population ρ_{33} (0) = α of the upper level and the splitting frequency δ of the doublet. This returned a number of interesting regularities of the time dynamics of the amplitudes of the electric field of SR and elements of the density matrix: Re[E(τ)] ≠ 0, Im[E(τ)] = 0; the real parts of high-frequency coherences Re[R_{31}(τ)] and Re[R_{32} (τ)] show a similar behavior, whereas their imaginary parts Im[R_{31}(τ)] and Im[R_{32} (τ)] exhibit an antiphase behavior. In accordance with this, the squares of their moduli, $|R_{31}|^2 = |R_{32}|^2$, evolve identically. The dynamics of populations ρ_{11}(τ) and ρ_{22}(τ) are identical and repeat the dynamics of superradiance field intensity $|E|^2$ (Ryzhov et al. 2017). This makes it possible to considerably simplify the mathematical model of the problem under consideration.

By introducing the notation

$$Re\left[E\right]=\epsilon, \quad Im\left[E\right]=0, \quad \rho_{21}=\eta+i\chi, \tag{9a}$$

$$\rho_{11}=\rho_{22}=\left(1-\rho_{33}\right)/2, \quad \rho_{33}=\alpha-\epsilon^2, \tag{9b}$$

$$\begin{aligned} Re\left[R_{31}\right]&=Re\left[R_{32}\right]=\xi,\\ Im\left[R_{31}\right]&=-Im\left[R_{32}\right]=\zeta,\\ \left|R_{31}\right|^2&=\left|R_{32}\right|^2=\xi^2+\zeta^2, \end{aligned} \tag{9c}$$

we can transform the system of differential equations (3) into the following system:

$$\dot{\epsilon}=2\xi, \tag{10a}$$

$$\dot{\xi}=-\frac{\delta}{2}\zeta+\frac{1}{2}\left(3\alpha-1\right)\epsilon-\frac{3}{2}\epsilon^3-\epsilon\eta, \tag{10b}$$

$$\dot{\zeta}=-\frac{\delta}{2}\xi-\epsilon\chi, \tag{10c}$$

$$\dot{\eta}=\delta\chi+2\epsilon\xi, \tag{10d}$$

$$\dot{\chi}=-\delta\eta+2\epsilon\zeta. \tag{10e}$$

Therefore, the relations (9) implement the reduction of our model from the complex domain to the real one. As a consequence, initial phase space R^{11} (3) of the model is completely mapped into R^5 (10). In addition, taking into account (4b) and relations (9), integral of motion (4c) takes the form

$$\begin{aligned} &\left(\epsilon^2-\gamma\right)^2+\frac{4}{3}\left(\eta^2+\chi^2+2\xi^2+2\zeta^2\right)=const,\\ &const=\frac{4}{3}\left(\alpha^2-\gamma^2+2R_0^2\right), \quad \gamma=\alpha-\frac{1}{3}. \end{aligned} \tag{11}$$

 https://www.doi.org/10.33910/2687-153X-2022-3-2-66-74

It is important to note that this law of conservation restricts the domain of existence of phase trajectories of the system and determines a closed hypersurface in the phase space (ϵ, ξ, ζ, η and χ) outside of which solutions of the system of equations (10) do not exist at any values of parameters α and δ. This makes it possible to characterise the process of SR as a process that is stable in the sense of Lagrange (Kuznetsov 2001). Topological specific features of hypersurface (11) depend on the sign of constant γ. First, $1 \geq \alpha > \frac{1}{3}$, i. e., at γ > 0, this is a five-dimensional "dumbbell" with symmetry axis $\boldsymbol{\epsilon}$. Second, if i. e., γ > 0, the hyper-surface is a five-dimensional ellipsoid. In the first variant, in the phase space of the system (under the condition α 1/3), there is hyperbolic chaos related with unpredictable abrupt transitions of the representing points between the family of torus lying in different cavities of "dumbbells". The movement of the phase space takes place on the surface of those tori. In the second case (α → 0), hyperbolic chaos is also present, but the family of tori already lying in the elliptical phase space intersects themselves in many ways, creating conditions that Puankare defined as a homoclinic structure (Puankare 1972; Ryzhov et al. 2017) of dynamic chaos.

Degenerate doublet

Let us consider a particular case of a degenerate doublet (δ = 0). In this limit, the system of differential equations (10) is considerably simplified and takes the form

$$\dot{\epsilon} = 2\xi, \quad \dot{\eta} = 2\epsilon\xi, \tag{12a}$$

$$\dot{\chi} = 2\epsilon\zeta, \quad \zeta = -\epsilon\chi, \tag{12b}$$

$$\dot{\xi} = \frac{1}{2}(3\alpha - 1)\epsilon - \frac{3}{2}\epsilon^3 - \epsilon\eta. \tag{12c}$$

This system of equations has integrals of motion. First, Eq. (12a) along with the initial conditions ϵ (0) = 0 and η (0) = – (1–α)/2 yield the first integral of motion:

$$2\eta - \epsilon^2 = \alpha - 1. \tag{13}$$

Second, Eq. (12b) and the initial conditions χ(0) = ζ(0) = 0 yield the second integral of motion: $\chi^2 + 2\zeta^2 = 0$, which means that functions χ(τ) and ζ(τ), which are defined in the real domain, remain unchanged and equal to zero within the entire SR process: χ(τ) = ζ(τ) = 0, τ ≥ 0. Then, expressing functional dependence η(ϵ) from (13) via ϵ^2 and substituting it into (12c), we obtain

$$\dot{\epsilon} = 2\xi, \tag{14a}$$

$$\dot{\xi} = \alpha\epsilon - 2\epsilon. \tag{14b}$$

Eliminating variable ξ from (14), we arrive at the following closed equation for the field ϵ (15)

$$\ddot{\epsilon} - 2\alpha\epsilon + 4\epsilon^3 = 0, \quad 1 \geq \alpha > 0, \tag{15}$$

which represents the Duffing equation (Duffing 1918) for an oscillator with a cubic nonlinearity without friction and external driving force. Eq. (15) yields the third integral of motion:

$$\frac{1}{2}\dot{\epsilon}^2 + V(\epsilon) = e, \tag{16}$$

the physical meaning of which is that it corresponds to the total energy of the oscillator (superradiance field), where, taking into account the initial conditions ϵ(0) = 0 and ξ(0) = ±R_0 ≠ 0, the value of the total energy is $e = 2R_0^2 > 0$ ($R_0 \neq 0$), while the function $V(\epsilon) = \epsilon^4 - \alpha\epsilon^2$ can be interpreted as a potential energy of SR. The relation between the signs in front of the linear and nonlinear terms in (15) characterises the SR field as that of a stable oscillation process in double-humped potential V(ϵ) with infinite walls, which has three singular points in the phase space $(\epsilon, \dot{\epsilon})$: $A_{1,2}\left(\pm\sqrt{\alpha/2}, -\alpha^2/4\right)$ are the points of a stable equilibrium of the centre type (minima of the potential V(ϵ)); and O(0,0) is the point of an unstable equilibrium of the saddle type (maximum of the potential V(ϵ)).

In the general case, $\xi(0)=R_0 \neq 0$, the value of total energy e (16) is always positive, $2R_0^2 > 0$. Consequently, the oscillation process of superradiance is always supernonlinear. In this case, Eq. (16) will have an exact solution. In terms of the elliptic functions, it can be obtained by applying the following substitution:

$$\epsilon = \epsilon_1 cos\left[\varphi\right], \qquad \epsilon_1^2 = \frac{\alpha}{2} + \sqrt{\frac{\alpha}{2} + 2R_0^2}$$

Then,

$$\varphi = am\left[\left(\phi\tau - \tau_d\right); m\right], \qquad \epsilon\left(\tau\right) = \epsilon_1 cn\left[\left(\phi\tau - \tau_d\right); m\right],$$

$$\tau_d = K\left(m\right), \qquad \phi = \sqrt{2\alpha + \frac{8R_0^2}{\epsilon_1^2}}, \tag{17}$$

$$T = 4K\left(m\right), \qquad m^2 = 1 - \frac{2R_0^2}{4R_0^2 + \alpha\epsilon_1^2},$$

where am[τ'; m] is the amplitude of Jacobi functions; cn[τ'; m]is the elliptic cosine; $\tau' = \phi\tau - \tau_d$, where τ_d is the delay time of the SR pulse (initial stage of SR); *K(m)* is the complete elliptic integral of the first kind; and *T* is the period of oscillations of the electric field strength. In this case, the physical picture of superradiance is rather transparent. From Eq. (14a), we have $\dot{\epsilon}\left(0\right) = \pm 2\xi\left(0\right) = \pm R_0$. If $\xi(0) = R_0$, then $\dot{\epsilon}\left(\tau\right) = \sqrt{2\left[e - V\left(\epsilon\right)\right]}$ and the field of superradiance will increase $(\dot{\epsilon}\left(\tau\right) > 0)$ in the time interval $0 \le \tau < T/4$ with delay τ_d; after that, the field will decrease within the interval of the same length, initiating a superradiance pulse. Upon the reverse motion, the system emits an antiphase pulse, and this process is periodically reproduced, since the system is conservative. If $\xi(0) = -R_0$ and $\dot{\epsilon}\left(\tau\right) = -\sqrt{2\left[e - V\left(\epsilon\right)\right]}$, the field of superradiance has a phase shift by $T/2 = \pi$.

Non-degenerate doublet

Eq. (3) has a numerical solution to study the dynamics of SR. For simplicity, the dipole moments of optical transitions were assumed to be equal: $d_{31} = d_{32} = 1$. Natural frequency of the resonator was chosen as the average between the frequencies of the high-frequency channels $\omega = (\omega_{31} + \omega_{32})/2$.

The calculations were carried out under the following initial conditions: $\rho_{11}(0) = \rho_{22}(0) = 0.4$, $\rho_{33}(0) = 0.2$, $\rho_{21}(0) = -0.4$, $R_{31}(0) = R_{32}(0) = 10^{-8}$, $E(0) = 0$. We can observe that there is no population inversion in the optical channels. At the same time, the inversion between the upper and the active state is 0.2. Non-zero values of $R_{31}(0)$ and $R_{32}(0)$ are required to initiate SR. The periodical regime of SR is observed without splitting doublet condition (see Fig. 2a) described by nonlinear equation (15) with cubic nonlinearity which was previously discussed. The splitting of the lower doublet $\omega_{21} \neq 0$ leads to the appearance of temporal modulation of the SR signals (Figs. 2b, 2c). This is due to the fact that with a nonzero splitting of the lower doublet, the states $|+\rangle$ and $|-\rangle$ are not stationary and, over time, the active state is periodically transformed into a passive one. In addition, a small change in the parameter of doublet splitting $\delta = 0.05 \leftrightarrow \delta = 0.1$ results in a complete change of the SR generation conditions. The transformation of an active state into a passive one leads to hyperbolic chaos in the system or the chaos of collapsing tori. Figs. 2b, 2c show variants of hyperbolic chaos. The time and amplitude characteristics of finding the system on the surface of one torus can vary unpredictably from those on another torus.

 https://www.doi.org/10.33910/2687-153X-2022-3-2-66-74

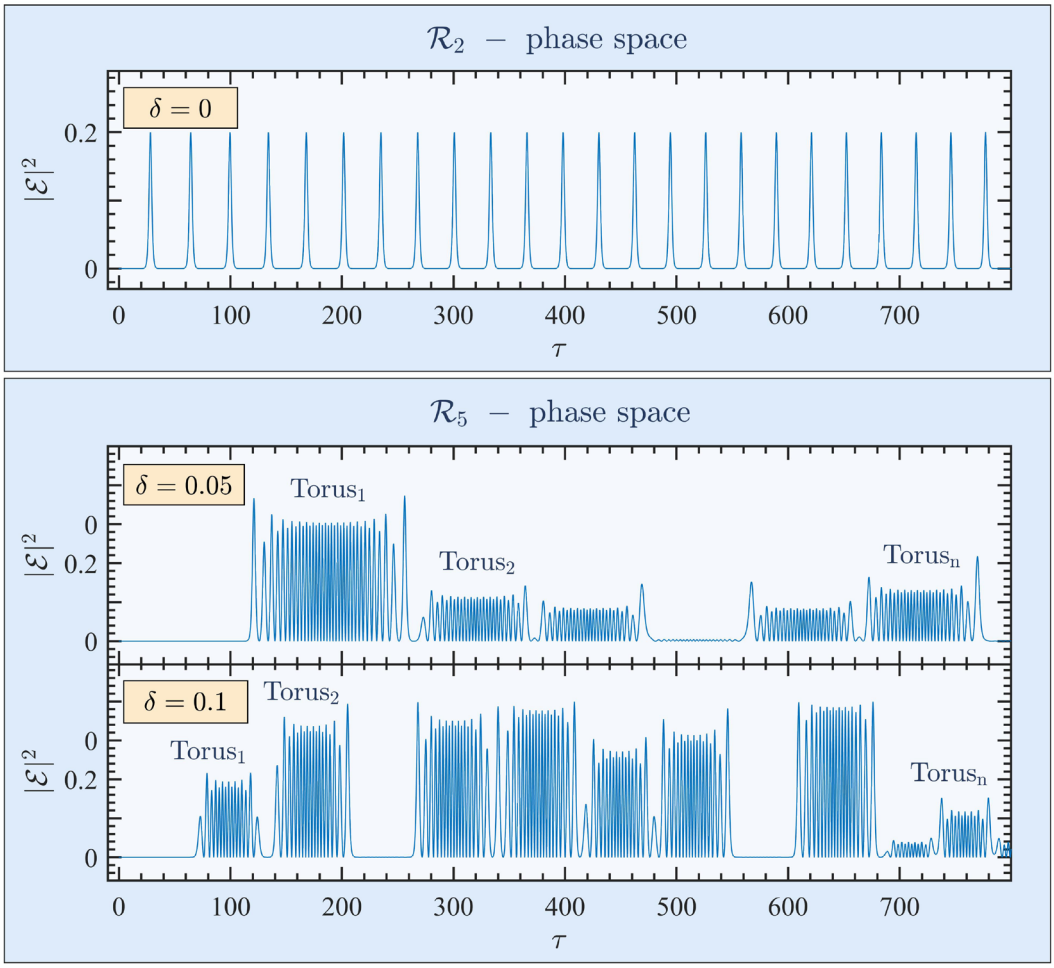

Fig. 2. Dynamics of SR without inversion of different values of the doublet splitting ω_{21}

Conclusions

For multilevel systems, in particular, for systems with the Λ-scheme of operating transitions, we showed that, at any population of the upper level, even without the inversion population on the whole, it is possible to initiate the generation of an SR pulse. The analysis of the new collective basis of the doublet state resulted in the development of conservation laws, which made it possible to considerably reduce the dimension of the phase space of the examined model ($R^{11} \to R^5 \to R^2$) and to realise conversion of the model from the complex to the real domain. We show that the system is marked by hyperbolic chaos.

Conflict of Interest

The authors declare that there is no conflict of interest, either existing or potential.

References

Andreev, A. V., Emel'yanov, V. I., Il'inskii, Yu. A. (1993) *Cooperative effects in optics*. Bristol: IOP Publ., 470 p. (In English).

Andreev, A. V., Emel'yanov, V. I., Il'inskii, Yu. A. (1980) Kollektivnoe spontannoe izluchenie (sverkhizluchenie Dike) [Collective spontaneous emission (Dicke superradiance)]. *Uspekhi fizicheskikh nauk — Physics–Uspekhi*, 131 (8), 653–694. https://doi.org/10.3367/UFNr.0131.198008d.0653 (In Russian)

Benedict, M. G., Ermolaev, A. M., Malyshev, V. A. et al. (1996) *Super-radiance: Multiatomic coherent emission*. New York: CRC Press, 338 p. https://doi.org/10.1201/9780203737880 (In English)

Bonifacio, K., Schwendimann, P., Haake, F. (1971) Quantum statistical theory of superradiance. *Physical Review A*, 4 (1), article 302. https://doi.org/10.1103/PhysRevA.4.302 (In English)
Bonifacio, R., Lugiato, L. A. (1975) Cooperative radiation processes in two-level systems: Superfluorescence. *Physical Review A*, 11 (5), article 1507. https://doi.org/10.1103/PhysRevA.11.1507 (In English)
Carlson, N. W., Jackson, D. J., Schawlow, A. L. et al. (1980) Superradiance triggering spectroscopy. *Optics Communications*, 32 (2), 350–354. https://doi.org/10.1016/0030-4018(80)90140-6 (In English)
Dicke, R. H. (1954) Coherence in spontaneous radiation processes. *Physical Review A*, 93 (1), 99–110. (In English)
Duffing, G. (1918) *Erzwungene Schwingungen bei veränderlicher Eigenfrequenz und ihre technische bedeutung [Forced vibrations with variable frequency and their technical importance]*. Braunschweig: University of California Libraries Publ., 134 p. (In German)
Gross, M., Haroche, S. (1982) Superradiance: An essay on the theory of collective spontaneous emission. *Physics Reports*, 93 (5), 301–396. https://doi.org/10.1016/0370-1573(82)90102-8 (In English)
Harris, S. E. (1989) Lasers without inversion: Interference of lifetime-broadened resonances. *Physical Review Letters*, 62 (9), article 1033. https://doi.org/10.1103/PhysRevLett.62.1033 (In English)
Kalachev, A. A., Samartsev, V. V. (2003) *Kogerentnye yavleniya v optike [Coherent phenomena in optics]*. Kazan: Kazan State University Publ., 281 p. (In Russian)
Kocharovskaya, O. A., Khanin, Ya. I. (1988) Kogerentnoe usilenie ul'trakorotkogo impul'sa v trekhurovnevoj srede bez inversii naselennostej [Coherent amplification of an ultrashort pulse in a three-level medium without a population inversion]. *Pis'ma v ZhETF — JETP Letters*, 48 (11), 581–584. (In Russian)
Kocharovskaya, O. (1997) Lasing without inversion: problems and prospects. In: *Hyperfine Interactions. The final proceedings for First international gamma-ray laser workshop. Vol. 107*. Bucharest: Institute of Atomic Physics-IFTAR Publ., pp. 187–197. https://doi.org/10.1023/A:1012072209659 (In English)
Kocharovskaya, O., Mandel, P. (1990) Amplification without inversion: The double-Λ scheme. *Physical Review A*, 42 (1), article 523. https://doi.org/10.1103/PhysRevA.42.523 (In English)
Kuznetsov, S. P. (2001) *Dinamicheskij khaos [Dynamic chaos]*. Moscow: Fizmatlit Publ., 595 p. (In Russian)
MacGillivray, J. C., Feld, M. S. (1976) Theory of superradiance in an extended, optically thick medium. *Physical Review A*, 14 (3), article 1169. https://doi.org/10.1103/PhysRevA.14.1169 (In English)
MacGillivray, J. C., Feld, M. S. (1981) Limits of superradiance as a process for achieving short pulses of high energy. *Physical Review A*, 23 (3), article 1334. https://doi.org/10.1103/PhysRevA.23.1334 (In English)
Malikov, R. F., Trifonov, E. D. (1984) Induced superradiance in activated crystals. *Optics Communications*, 52 (1), 74–76. https://doi.org/10.1016/0030-4018(84)90076-2 (In English)
Malyshev, V. A., Ryzhov, I. V., Trifonov, E. D., Zaitsev, A. I. (1998) Superradiance without inversion. *Laser Physics*, 8 (2), 494–497. (In English)
Malyshev, V. A., Carreno, F., Anton, M. A. et al. (2003) Superradiance from an ultrathin film of three-level V-type atoms: Interplay between splitting, quantum coherence and local-field effects. *Journal of Optics B: Quantum and Semiclassical Optics*, 5 (3), article 313. https://doi.org/10.1088/1464-4266/5/3/318 (In English)
Malyshev, V. A., Ryzhov, I. V., Trifonov, E. D., Zaitsev, A. I. (2000) Super-radiance from a thin solid film of three-level atoms: Local-field effects. *Optics Communications*, 180 (1–3), 59–68. https://doi.org/10.1016/S0030-4018(00)00678-7 (In English)
Puankare, A. O. (1972) *Izbrannye trudy: v 3 t. T. 2 [Selected works: In 3 vols. Vol. 2]*. Moscow: Nauka Publ., 998 p. (In Russian)
Rehler, N. E., Eberly, J. H. (1971) Superradiance. *Physical Review A*, 3 (5), article 1735. https://doi.org/10.1103/PhysRevA.3.1735 (In English)
Ryzhov, I. V., Vasil'ev, N. A., Kosova, I. S. et al. (2017) Kooperativnoe izluchenie ansamblya trekhurovnevykh Λ-izluchatelej v rezonatore: vzglyad s tochki zreniya dinamiki nelinejnykh sistem [Cooperative emission from an ensemble of three-level Λ radiators in a cavity: An insight from the viewpoint of dynamics of nonlinear systems]. *Zhurnal eksperimental'noj i teoreticheskoj fiziki — Journal of Experimental and Theoretical Physics*, 151 (5), 803–822. (In Russian)
Ryzhov, I. V., Zaitsev, A. I., Shuval-Sergeeva, E. V. (2012) Superradiance of the system comprised of two parallel resonant thin layers. *Optics and Spectroscopy*, 112 (4), 604–611. https://doi.org/10.1134/S0030400X12040182 (In English)
Scully, M. O. (1992) From lasers and masers to phaseonium and phasers. *Physics Reports*, 219 (3–6), 191–201. https://doi.org/10.1016/0370-1573(92)90136-N (In English)
Sokolov, I. V., Trifonov, E. D. (1974) Collective spontaneous emission by polyatomic systems. *Journal of Experimental and Theoretical Physics*, 38 (1), 37–40. (In English)
Yuan, L., Svidzinsky, A. A. (2012) Gain without population inversion in a yoked superfluorescence scheme. *Physical Review A*, 85 (3), article 033836. https://doi.org/10.1103/PhysRevA.85.033836 (In English)
Zaitsev, A. I., Ryzhov, I. V., Trifonov, E. D. et al. (1999) Superradiance without inversion in a thin layer of three-level atoms. *Laser Physics*, 9 (4), 876–888. (In English)
Zheleznyakov, V. V., Kocharovskij, V. V., Kocharovskij, V. V. (1989) Volny polyarizatsii i sverkhizluchenie v aktivnykh sredakh [Polarization and superradiation waves in active media]. *Uspekhi fizicheskikh nauk* — Physics–*Uspekhi*, 159 (2), 193–260. https://doi.org/10.3367/UFNr.0159.198910a.0193 (In Russian)

Theoretical Physics. Cosmology

UDC 53.02+523.9

EDN KSMTED

https://www.doi.org/10.33910/2687-153X-2022-3-2-75-80

Thermoelectrokinetic phenomena in the convective plasma zone of the Sun and stars

V. M. Grabov✉[1], A. A. Zaitsev[2], D. V. Kuznetsov[2], A. V. Sidorov[2], E. Yu. Semenova[1]

[1] Herzen State Pedagogical University of Russia, 48 Moika Emb., Saint Petersburg 191186, Russia
[2] Bunin Yelets State University, 28 Communarov Str., Yelets 399770, Russia

Authors

Vladimir M. Grabov, ORCID: 0000-0003-0215-6474, e-mail: vmgrabov@yandex.ru

Andrey A. Zaitsev, ORCID: 0000-0003-3377-0805, e-mail: zaitsev@elsu.ru

Denis V. Kuznetsov, ORCID: 0000-0003-2156-4000, e-mail: kuznetcovdv007@mail.ru

Alexander V. Sidorov, ORCID: 0000-0003-4460-0414, e-mail: dirnusir@mail.ru

Elena Yu. Semenova, e-mail: phys@herzen.spb.ru

For citation: Grabov, V. M., Zaitsev, A. A., Kuznetsov, D. V., Sidorov, A. V., Semenova, E. Yu. (2022) Thermoelectrokinetic phenomena in the convective plasma zone of the Sun and stars. *Physics of Complex Systems*, 3 (2), 75–80. https://www.doi.org/10.33910/2687-153X-2022-3-2-75-80. EDN KSMTED.

Received 18 March 2022; reviewed 15 April 2022; accepted 20 April 2022.

Funding: The study is part of the State-Commissioned Assignment of the Ministry of Education of Russia, project No. FSZN-2020-0026.

Abstract. The study shows that electromagnetic phenomena in the convective plasma zone of the Sun and stars and the local magnetic field near the Sun's surface are caused not only by the magnetohydrodynamic dynamo mechanism (Krause, Rädler 1980; Moffatt 1978; Morozov 2006), but also by the phenomena that have relatively recently become the focus of research, i. e., thermoelectrokinetic phenomena in the viscous electrically conductive medium in the presence of a temperature gradient (Grabov 2003; 2005a; 2005b; Prigogine, Nicolis 1977). The results of physical modelling and quantitative estimates show that thermoelectrokinetic currents can create primary magnetic fields of approximately B ≅ 103 Gs in the convective plasma zone of the Sun and stars.

Keywords: thermoelectrokinetic phenomena, viscous electrically conductive substance, plasma of the Sun, convective zone of the Sun, magnetic field near to a surface of the Sun

Introduction

Usually, electromagnetic processes in the convective plasma zone of the Sun and stars are described on the basis of the theory of magnetohydrodynamic dynamo (Krause, Rädler 1980; Moffatt 1978; Morozov 2006) (see Fig. 1 and Fig. 2). As the authors note (Krause, Rädler 1980), this theory is based on the equations of magnetic hydrodynamics: Maxwell's equations, the corresponding equations of the state and the Navier—Stokes equation. The most important value in the electrodynamics of medium fields is the average value of the electromotive force arising from the interaction of the velocity fluctuation and the magnetic field.

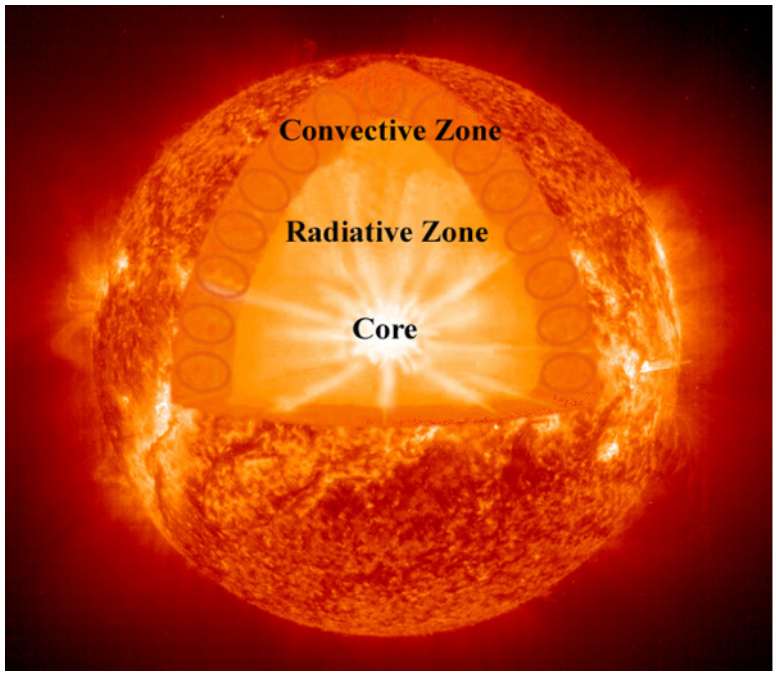

Fig. 1. Convective zone of the Sun

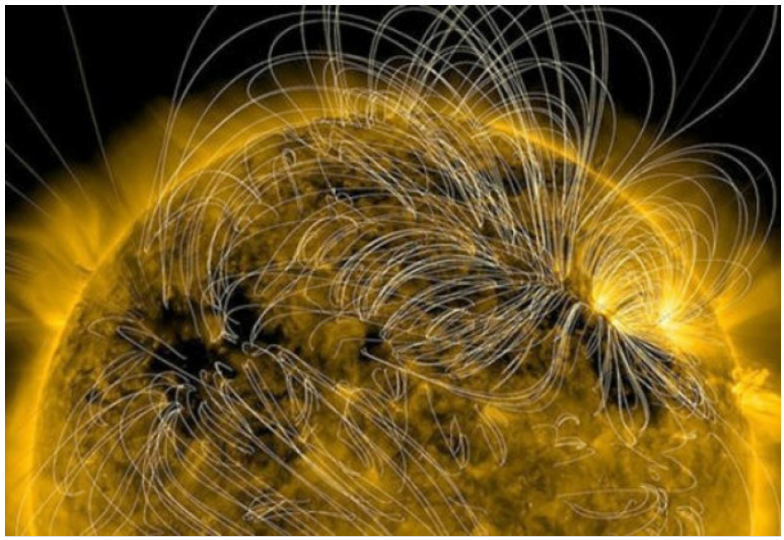

Fig. 2. Local magnetic field near to a surface of the Sun

The convective plasma zone of the Sun and stars is located in the gravitation field and the field of the radial temperature gradient. Along with that, the convective flow system itself is represented by convective dissipative structures such as Benard cells resulting from self-organisation in viscous media under conditions far from thermodynamic equilibrium (Ebeling 1976; Prigogine, Nicolis 1977).

On the other hand, it is known that in plasma, under the action of the temperature gradient and due to the differences in the intensity of thermodiffusion of electrons and ions, the thermoelectric field with the strength is formed (Kotel'nikov 2013).

$$E_t = \frac{3}{2}\left(\frac{k}{e}\right)\nabla T \tag{1}$$

In the presence of inhomogeneity of the medium, the thermoelectric electromotive force is formed (Anatychuk 1998):

$$\varepsilon = \oint (E_t dl) \neq 0 \tag{2}$$

 https://www.doi.org/10.33910/2687-153X-2022-3-2-75-80

We will discuss the possibility of forming thermoelectric EMF in the convective plasma zone of the Sun and stars. It is obvious that this zone is located in the field of the radial temperature gradient in the state of existing closed thermokinetic vortices. Their model can be represented as a toroidal vessel filled with the viscous electrically conductive substance located in the field of parallel vectors of gravitational force and temperature gradient, as shown in Fig. 3.

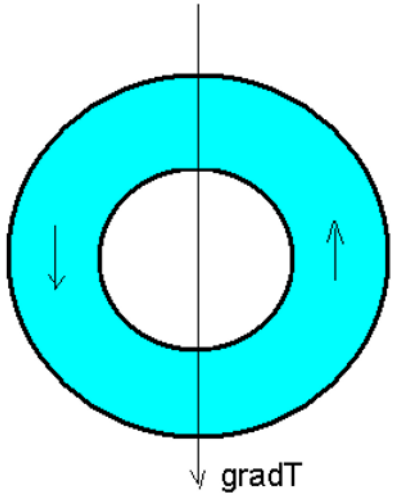

Fig. 3. Toroid as a vortex model convective cell

The theoretical analysis (Landa 2010) shows that if the Rayleigh number increases higher than the critical value, an ordered move, whose direction is determined by random factors, occurs in the vessel.

A further development of the toroid model (Fig. 3) is the transition to the open flow system in the form of a U-shaped tube through which a viscous electrically conductive liquid flows at the velocity V. It can be considered an analogue of the open semiconductor thermoelectric element, see Fig. 4.

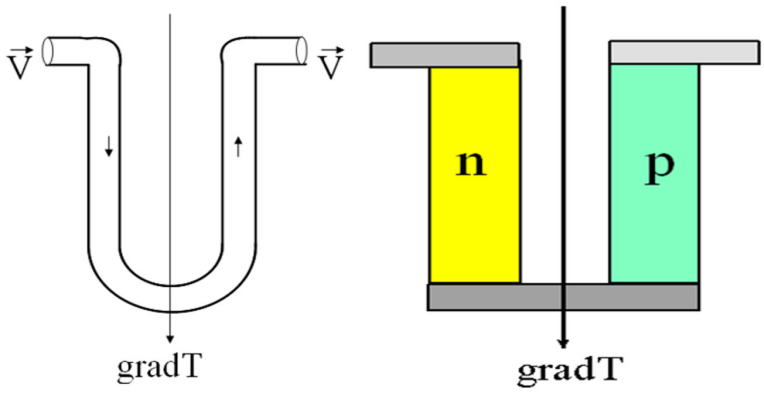

Fig. 4. The open flow system as an analog of a semiconductor thermoelectric element

The thermoelectric EMF in the viscous electrically conductive substance caused by this kinetic inhomogeneity was termed thermoelectrokinetic EMF (Grabov 2003; 2005a; 2005b; Grabov et al. 2010; 2017; Zaitsev et al. 2015). It belongs to the new group of thermoelectrokinetic phenomena that have become the focus of detailed experimental and theoretical research with the evidence taken from aqueous solutions of ionic compounds and electrolytes (Grabov et al. 2010; 2017; Zaitsev et al. 2015).

The experimental study of new thermoelectrokinetic phenomena

Experimental studies of thermoelectrokinetic EMF in liquid electrolytes was carried out using the equipment developed by (Grabov et al. 2010; 2017; Zaitsev et al. 2015) (see the layout in Fig. 5). Liquid electrolytes, aqueous solutions of ionic compounds, acids, alkalis and salts were used as a viscous electrically conductive medium. To get large values of thermoelectric EMF coefficients, the mobility of positive and negative ions in the solution should have significantly different values (Grabov et al. 2010; Zaitsev et al. 2015). These requirements are met, for example, by an aqueous solution of potassium hydroxide (KOH) with the mobility of K+ ions (7.6×10^{-8} $m^2V^{-1}c^{-1}$) and OH- (20.5×10^{-8} $m^2V^{-1}c^{-1}$) at 25 °C and the coefficient of thermoelectric EMF ε = –0.6 mV/K (Grabov et al. 2010; Zaitsev et al. 2015).

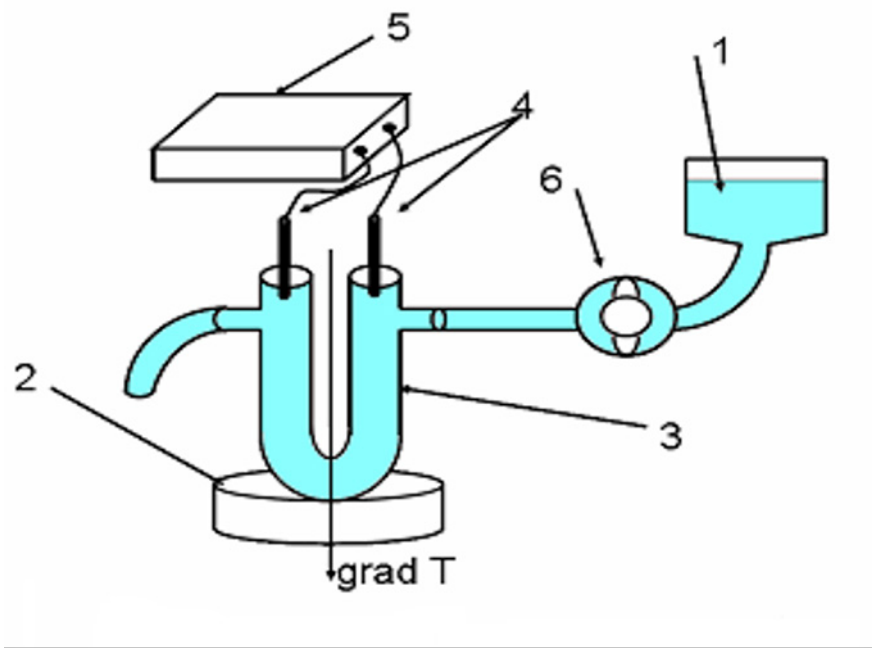

1—electrolyte, 2—heater, 3—U-shaped tube, 4—electrodes, 5—electrical measuring instrument, 6—peristaltic pump.

Fig. 5. Equipment for measuring thermoelectrokinetic EMF in liquid electrolytes

The thermoelectrokinetic EMF was measured between the points of entrance and exit of the electrolyte. The temperature was maintained the same throughout the experiment. In the presence of a temperature gradient and the absence of electrolyte flow, the EMF was close to zero, since the branches of the thermoelement were symmetrical. During electrolyte flow, the symmetry of the branches was violated, as a result, the EMF was measured and was found proportional to the temperature difference and the solution concentration. The dependence on electrolyte flow rate was linear at the initial stage, then it passed through a maximum with an EMF coefficient value approximately equal to 0.1 mV/K (Grabov et al. 2010; 2017; Zaitsev et al. 2015). This was due to a decrease in heat exchange and a temperature drop.

The experiments showed that the thermoelectrokinetic field strength and the thermoelectrokinetic EMF are proportional to the thermoelectric coefficient of the solution (α), temperature gradient (gradT) and the solution flow density (nv).

$$E = \beta(\alpha gradT)(nv) \tag{3}$$

$$\varepsilon_{TEK} = \oint \beta(\alpha gradT)(nv)\,dl \tag{4}$$

At the fixed optimal electrolyte flow rate, the strength of the thermoelectrokinetic field is proportional to the temperature gradient (5) with the coefficient γ ≈ 0.1 mV/K for potassium hydroxide (KOH) (Grabov et al. 2010; Zaitsev et al. 2015).

 https://www.doi.org/10.33910/2687-153X-2022-3-2-75-80

$$E = -\beta\left(\alpha gradT\right)\left(nv\right) = -\gamma gradT \tag{5}$$

Let us apply the toroid model to the plasma convective vortex flow in the convective zone of the Sun (Grabov, Zaitsev, Kuznetsov 2012) (see Fig. 3). Let the external diameter of the convective zone of the Sun amount to about 10^4 km, a toroid cross-section dimeter to about 3×10^3 km, plasma conductivity equal $\sigma = 3 \times 10^3$ Ohm^{-1}m^{-1}, the average temperature value equal gradT = 10^{-2} K/m (Krause, Rädler 1980; Moffatt 1978; Morozov 2006) and the thermoelectrokinetic field strength coefficient equal the value obtained in the experiment with electrolytes γ = 0.1mV/K (Grabov et al. 2010; Zaitsev et al. 2015). Then, the magnitude of the magnetic induction vector in the toroid center, see Fig. 6, is 0.1 Tl, which is close in magnitude order to the experimentally observed results in the region of sunspots. This magnetic field can be considered as primary in plasma, as the dissipative substance which is transformed in magneto-hydrodynamic processes and makes up a large range of observed values of magnetic field induction in the convective zone of the Sun. The magnetic field B ≅ (10 – 10^3) Gs is observed experimentally in sunspots (Krause, Rädler 1980; Moffatt 1978; Morozov 2006).

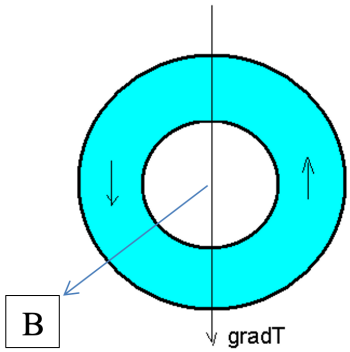

$E = \gamma\, gradT$
$\gamma = (0{,}1 - 1)$ mV/K
$E = \gamma\, gradT = 10^{-5}$ V/m
$J = \sigma E = 10^{-2}$ A/m^2
$I = JS = J(\pi d^2/4) \cong 10^{11}$ A
$B = \mu_0 I/2\pi R \cong 10^{-1}$ T $\cong 10^3$ Gs

Fig. 6. Electric current and magnetic field of a single cell of the convective zone of the Sun

There is a reason to believe that thermoelectrokinetic phenomena can form in the viscous bowels of planets, their atmospheres and oceans.

Conclusions

The new class of phenomena in viscous electrically conductive media, called thermoelectrokinetic, has been experimentally discovered. These phenomena are cross kinetic phenomena of electric charge transfer in the presence of mass transfer and internal energy transfer.

Thermoelectrokinetic EMF and closed electric currents are formed in convective plasma cells in the convective zone of the Sun.

Approximate estimates show that the thermoelectrokinetic currents can create primary magnetic fields in the convective zone of the Sun which are transformed during the magnetohydrodynamic processes and make up a large range of the observed values of magnetic field induction.

Thermoelectrorinenic phenomena play a significant role in the evolution of the surrounding world.

Conflict of Interest

The authors declare that there is no conflict of interest, either existing or potential.

References

Anatychuk, L. I. (1998) *Thermoelectricity. Vol I. Physics of Thermoelectricity*. Kiev: Institute of Thermoelectricity Publ., 376 p. (In English)

Ebeling, W. (1976) *Strukturbildung bei irreversiblen Prozessen: Eine Einführung in die Theorie dissipativer Strukturen [Formation of structures in irreversible processes: An introduction to the theory of dissipative structures]*. Teubner: Verlag Leipzig, 194 p. (In German)

Grabov, V. M. (2003) Nonequilibrium thermodynamics and thermoelectric phenomena. *Journal of Thermoelectricity*, 3, 5–12. (In English)

Grabov, V. M. (2005a) Thermoelectrokinetic and thermoelectromagnetic phenomena under far from thermodynamic equilibrium conditions. *Journal of Thermoelectricity*, 2, 44–51. (In English)

Grabov, V. M. (2005b) On one of promising directions in the development of fundamental physics of thermoelectricity in XXI century. *Journal of Thermoelectricity*, 4, 59–62. (In English)

Grabov, V. M., Sidorov, A. V., Zaitsev, A. A., Kuznetsov, D. V. (2017) Modelirovanie protsessov nestatsionarnogo teplomassoperenosa v vodnykh rastvorakh sil'nykh elektrolitov [Modeling of unsteady heat and mass transfer processes in aqueous solutions of strong electrolytes]. In: *Neobratimye protsessy v prirode i tekhnike: trudy devyatoj Vserossijskoj konferentsii, 25–27 yanvarya 2017 goda [Irreversible processes in nature and technology: Proceedings of the 9th All-Russian Conference, January 25–27, 2017]*. Moscow: Bauman University Publ., pp. 251–256. (In Russian)

Grabov, V. M., Zaitsev, A. A., Kuznetsov, D. V. (2010) Thermoelectric and thermoelectrokinetic phenomena in aqueous solutions of ionic compounds. *Journal of Thermoelectricity*, 1, 39–48. (In English)

Grabov, V. M., Zaitsev, A. A., Kuznetsov, D. V. (2012) Fizicheskoe modelirovanie elektromagnitnykh yavlenij v konvektivnoj zone Solntsa [Physical modeling of electromagnetic phenomena in the convective zone of the Sun]. In: *Materialy XVI Vserossijskoj ezhegodnoj konferentsii po fizike Solntsa "Solnechnaya i solnechno-zemnaya fizika 2012" [Materials of the XVI All-Russian Annual Conference on Solar Physics "Solar and Solar-Earth Physics 2012"]*. Saint Peterburg: The Central Astronomical Observatory of the Russian Academy of Sciences at Pulkovo Publ., pp. 211–214. (In Russian)

Kotel'nikov, I. A. (2013) *Lektsii po fizike plazmy [Lectures on plasma physics]*. Moscow: BINOM. Laboratoriya znanij Publ., 384 p. (In Russian)

Krause, F., Rädler, K.-H. (1980) *Mean-field magnetohydrodynamics and dynamo theory*. Berlin: Academie Publ., 272 p. (In English)

Landa, P. S. (2010) *Nelinejnye kolebaniya i volny [Nonlinear oscillations and waves]*. Moscow: Librokom Publ., 552 p. (In Russian)

Moffatt, H. K. (1978) *Magnetic field generation in electrically conducting fluids*. Cambridge: Cambridge University Press, 325 p. (In English)

Morozov, A. I. (2006) *Vvedenie v plazmodinamiku [Introduction to plasmadynamics]*. Moscow: FIZMATLIT Publ., 576 p. (In Russian)

Prigogine, I., Nicolis, G. (1977) *Self-organization in non-equilibrium systems*. New York: J. Wiley & Sons Publ., 512 p. (In English)

Zaitsev, A. A., Grabov, V. M., Kuznetsov, D. V. (2015) Thermoelectrokinetic effect in viscous conductive media. *Indian Journal of Science and Technology*, 8 (Suppl. 10), 1–10. https://doi.org/10.17485/ijst/2015/v8iS10/84884 (In English)

Theoretical physics. Cosmology

UDC 524.8

EDN MWCGSM

https://www.doi.org/10.33910/2687-153X-2022-3-2-81-85

Non-linearity of Vaidya spacetime and forces in the central naked singularity

V. D. Vertogradov[✉1, 2]

[1] Herzen State Pedagogical University of Russia, 48 Moika Emb., Saint Petersburg 191186, Russia
[2] The Special Astrophysical Observatory of the Russian Academy of Sciences,
65 Pulkovskoe Highway, Saint Petersburg 196140, Russia

Authors

Vitalii D. Vertogradov, ORCID: 0000-0002-5096-7696, e-mail: vdvertogradov@gmail.com

For citation: Vertogradov, V. D. (2022) Non-linearity of Vaidya spacetime and forces in the central naked singularity. *Physics of Complex Systems*, 3 (2), 81–85. https://www.doi.org/10.33910/2687-153X-2022-3-2-81-85. EDN MWCGSM.

Received 22 February 2022; reviewed 28 March 2022; accepted 28 March 2022.

Funding: This study was conducted by SAO RAS as part of the State-Commissioned Assignment "Fundamental Scientific Research". The study was supported by the Russian Science Foundation, grant No. 22-22-00112.

Abstract. The paper focuses on non-linear Vaidya spacetime, i. e., cases when the mass function has a non-linear form $M(v) \equiv \lambda v^n$, $\lambda > 0$, $n > 1$. We prove that the central naked singularity might form for values $n > 1$, however, under such conditions it will be gravitationally weak. The paper also disucsses forces in the naked singularity and proves that they might be finite only in the case of the gravitationally weak naked singularity. It also focuses on the strength of the singularity. We prove that the strong naked singularity might form only in the linear case. The singularity might also be gravitationally strong in the case of black hole formation.

Keywords: Vaidya spacetime, naked singularity, strength of singularity, inertial forces, geodesics, gravitational collapse

Introduction

The Vaidya spacetime is one of the earliest counterexamples of cosmic censorship conjecture [CCC] violation (Vaidya et al. 1985). Vaidya spacetime is so-called radiating Schwarzschild metric with non-zero right hand-side of the Einstein equation. The energy-momentum tensor in Vaidya spacetime represents the null dust and has the following form:

$$T_{ik} = \rho \delta_i^0 \delta_k^0 , \tag{1}$$

where ρ is the energy density of this null dust.

The gravitational collapse of usual Vaidya spacetime (Dwivedi, Joshi 1989) might lead to the formaiton of the naked singularity. It means that there exist a family of non-spacelike future-directed geodesics which terminate in the central singularity in the past. Moreover, the time of the singularity formation must be shorter than the time of the apparent horizon formation. The geodesic motion represents the free movement. It means there is no any non-gravitational force acting on the particle. However, there are so-called inertial forces and the particle moves in the medium because this spacetime is filled with the null dust. We can calculate these forces and, as we see below, in the case of linear Vaidya spacetime (the mass function is the linear one) these forces are infinite. We will show that in the case of non-linear Vaidya spacetime these forces might be finite.

We will provide evidence that the naked singularity which is formed in the case of non-linear Vaidya spacetime is gravitationally weak. Let us consider Tipler's definition given in the paper (Nolan 1999): a singularity is termed to be gravitationally strong or simply strong if it destroys by stretching or crushing any object which falls into it. If it does not destroy any object this way, then the singularity is termed to be gravitationally weak.

The paper investigates the inertial forces in the case of the naked singularity formation and determines the conditions under which these forces might be finite. The paper also focuses on the strength of the singularity.

This paper is organised as follows: in Sec. II we consider the possibility of the naked singularity formation in the case $M(v) = \lambda v^n$, in Sec. III we consider the inertial forces in Vaidya spacetime. In Sec. IV we investigate the strength of the naked singularity in the case of non-linear Vaidya metric. Sec. V is the conclusion.

Throughout the paper the system of units $c = G = 1$will be used.

Naked singularity formation

The usuall Vaidya spacetime has the following form:

$$ds^2 = -\left(1 - \frac{2M(v)}{r}\right)dv^2 + 2\varepsilon dv dr + r^2 d\Omega^2, \tag{1}$$

where ε = ± 1is ingoing (outgoing) radiation, $M(v)$ is the mass function, and $v_{\pm 1}$ is advanced (retarded) Edington's time. $d\Omega$ is the metric on the unit two-sphere:

$$d\Omega_2 \equiv d\theta_2 + sin_2\, \theta d\phi_2. \tag{2}$$

Our case is related to the gravitational collapse, hence, we will use ε = +1 throughout the paper.

The case $M(v) = \lambda v^n$

Let us consider the case when the mass function has the form:

$$M(v) = \lambda v^n, \tag{3}$$

where λ is a positive real constant.

The equation of the apparent horizon is given by (Poisson 2004):

$$g_{00} = \frac{2\lambda v^n}{r} - 1 = 0\ . \tag{4}$$

We can see that if $v = 0$, then we can not satisfy the apparent horizon equation (we need positive values of r).

At the time $v = 0$ and at the point $r = 0$ we have the singularity formation but for it to be naked there must be non-spacelike future-directed geodesics which terminate at the central singularity in the past. Let us consider the existence of radial null geodesics. The geodesic equation in this case is given by:

$$\frac{dv}{dr} = \frac{2r}{r - 2\lambda v^n}\ . \tag{5}$$

The geodesic can originate from the central singularity if $\lim\limits_{v\to 0, r\to 0} \frac{dv}{dr} = X_0$, where X_0 is a finite positive number.

We should consider 3 cases:

- $0 < N < 1$,
- $n = 1$,
- $n > 1$.

The case of linear mass function $n = 1$ has been considered in (Dwivedi, Joshi 1989). In this case we have the naked singularity formation if $\lambda < \frac{1}{8}$. Also, this singularity is gravitationally strong (Nolan 1999; Tipler 1977).

 https://www.doi.org/10.33910/2687-153X-2022-3-2-81-85

Let us consider the case $n < 1$. Let us denote $\lim_{v\to 0, r\to 0} \frac{dv}{dr} = X_0$, then

$$X_0 = \frac{2}{1-2\lambda n X_0 v^{n-1}}, \qquad (6)$$
$$2\lambda n v^{n-1} X_0^2 - X_0 + 2 = 0 .$$

$v \to 0$ and $n < 1$, hence, from the last equation we can see X_0 can not be positive real constant and $X_0 \to \infty$. We can conclude that, in this case, there are no radial null geodesics which terminate at the central singularity in the past.

Now, let us consider the case when $n > 1$. Thus, we have:

$$X_0 = \frac{2}{1-2\lambda n X_0 v^{n-1}}, \qquad (7)$$
$$2\lambda n v^{n-1} X_0^2 - X_0 + 2 = 0 .$$

Here, we have three possible options:

• $X_0 = 0$. In this case we do not have any uncertainty and the geodesic equation (7) gives impossible equality. So, this option is impossible.

• $X_0 \to \infty$. In this case the condition $\lim_{r\to 0\, v\to 0} v^{n-1} X_0 = \frac{1}{2\lambda n}$ must be held. However, the previous equation (7) gives impossible equality, which is why this option is also unacceptable.

• $X_0 = \mu$, where μ is real positive constant. In this case we have an equality $X_0 = 2$ and it is the only suitable option.

Note that here we have a radial null geodesic which terminates at the central singularity in the past regardless of value . Further we will show that in the case $n > 1$ this singularity is gravitationally weak.

The inertial forces

To investigate the inertial forces one should consider the second order geodesic equations. In Vaidya spacetime they are given by:

$$\frac{d^2t}{d\tau^2} = -\frac{M(v)}{r^2}\left(\frac{dt}{d\tau}\right)^2 + r\left(\frac{d\theta}{d\tau}\right)^2 + r\sin^2\theta\left(\frac{d\varphi}{d\tau}\right)^2 . \qquad (8)$$

$$\frac{d^2r}{d\tau} = -\frac{\left(1-\frac{2M(v)}{r}\right)M(v) + \dot{M}(v)r}{r^2}\left(\frac{dt}{d\tau}\right)^2 + 2\frac{M(v)}{r^2}\frac{dt}{d\tau}\frac{dr}{d\tau} \qquad (9)$$
$$+\left(r - M(v)\right)\left(\frac{d\theta}{d\tau}\right)^2 + \left(r - M(v)\right)\sin^2\theta\left(\frac{d\varphi}{d\tau}\right)^2 .$$

$$\frac{d^2\theta}{d\tau^2} = -\frac{2}{r}\frac{dr}{d\tau}\frac{d\theta}{d\tau} + \sin\theta\cos\theta\left(\frac{d\varphi}{d\tau}\right)^2 . \qquad (10)$$

$$\frac{d^2\varphi}{d\tau^2} = -\frac{2}{r}\frac{dr}{d\tau}\frac{d\varphi}{d\tau} - 2\cot\theta\frac{d\theta}{d\tau}\frac{d\varphi}{d\tau} . \qquad (11)$$

One should note that only the following combination of four-velocity $u^0\,u^0$ and $u^0\,u^\alpha$, α=1, 2, 3 gives us the inertial forces. The combination $u^\alpha\,u^\beta$ is the part of three covariant derivative and they are not forces at all (Landau, Lifshitz 1980).

Here we have 2 different forces $\Gamma^0_{00} = -\Gamma^1_{01} = \frac{M(v)}{r^2}$ and $\Gamma^1_{00} = \frac{\left(1-\frac{2M(v)}{r}\right)M(v) + \dot{M}(v)r}{r^2}$. We are interested in the case of the naked singularity formation. As we found out above, under the mass function $M(v) = \lambda v^n$, the gravitational collapse will result in the naked singularity when $n \geq 1$. Using the well-known formula (Landau, Lifshitz 1980):

$$u^{\alpha} = \frac{1}{\sqrt{1-\beta^2}} \frac{dx^{\alpha}}{dt},$$
$$u^{0} = \frac{1}{\sqrt{1-\frac{2\lambda v^n}{r}\left(1-\beta^2\right)}} - \frac{r}{\left(r-2\lambda v^n\right)\left(1-\beta^2\right)} \frac{dx^{\alpha}}{dt}, \tag{12}$$

we can easily obtain the radial force expression:

$$F^{r}_{cent} = -\frac{\left(1-\frac{2\lambda v^n}{r}\right)\lambda v^n + \lambda n v^{n-1} r}{r^2\left(1-\frac{2\lambda v^n}{r}\right)\left(1-\beta^2\right)},$$
$$F^{r}_{nc} = \frac{2}{\sqrt{1-\frac{2\lambda v^n}{r}\left(1-\beta^2\right)}}\left[\frac{\left(1-\frac{2\lambda v^n}{r}\right)\lambda v^n + \lambda n r v^{n-1}}{r^2} - \frac{\lambda v^n}{r^2}\right]\frac{dr}{dt}, \tag{13}$$

where F_{cent} is the centrifugal force and F_{nc} is the force which depends upon a velocity $\frac{dr}{dt}$ linearly. We know that when $n \geq 1$, then $\lim\limits_{r\to 0, v\to 0} \frac{dv}{dr} = X_0$, where X_0 is a positive real constant. Thus, to find the forces in the central naked singularity one should consider three cases:

1. $n \in [1, 2)$. In this case it is easy to see that we have infinity inertial forces:

$$\lim_{r\to 0,\ v\to 0} F^{r}_{cent}, = \infty$$
$$\lim_{r\to 0,\ v\to 0} F^{r}_{nc}. = \infty \tag{14}$$

2. $n = 2$. In this case we have:

$$\lim_{r\to 0,\ v\to 0} F^{r}_{cent} = -\frac{1}{1-\beta^2}\left(\left(\lambda X_0^2 + 2\lambda X_0\right)\right),$$
$$\lim_{v\to 0,\ r\to 0} F^{r}_{ns} = \frac{2}{1-\beta^2}\, 2\lambda X_0 \frac{dr}{dt}. \tag{15}$$

We can see that in this case the radial inertial forces have a real positive finite value.

3. $N > 2$. In this case all inertial forces equall zero.

The strength of the central singularity

According to Tipler's definition the singularity is strong if the following condition is held (Nolan 1999; Tipler 1977):

$$\lim_{\lambda\to 0} \lambda^2 R_{ik} K^i K^k = \xi > 0, \tag{16}$$

where λ is affine parameter, K^i is the tangent vector to the singularity, R_{ik} is the Ricci tensor. Besides, ξ must be finite. In the case of usual Vaidya spacetime the condition 1 gives for the expression ξ:

$$\xi = \frac{2\dot{M}(v)}{r^2} v^2. \tag{17}$$

We are interested in the case $M(v) = \lambda v^n$. One can obtain:

$$\xi = \frac{2n\lambda v^{n+1}}{r^2}. \tag{18}$$

 https://www.doi.org/10.33910/2687-153X-2022-3-2-81-85

Now we should consider the following limit (as in the previous cases we denote $\lim\limits_{v\to 0, r\to 0} \frac{dv}{dr} = X_0$):

$$\lim_{v\to 0} \xi = 2nv^{n-1}x_0^2 \ , \tag{19}$$

From this we can conclude that if $n = 1$, then we have gravitationally strong naked singularity. If $n > 1$, then $\xi = 0$ and we have only gravitationally weak naked singularity.

From this result we can conclude that in Vaidya spacetime, in the case of the naked singularity formation the inertial forces in this region are infinite when the singularity is gravitationally strong. When these forces have finite real value or are equal to zero, then the central singularity is gravitationally weak.

Conclusion

In this paper we have considered Vaidya spacetime when the mass function is $M(v) = \lambda v^n$. We found out that when $n \geq 1$, the result of the gravitational collapse might be the naked singularity. It means that there exist a family of non-spacelike future-directed geodesics which terminate in the central singularity in the past and the time of the apparent horizon is bigger than the time of the singularity formation. However, if there is such a family of geodesics, then particles can move along them and we investigated the question which inertial forces act on this particle when it escapes the naked singularity. We found out that these inertial forces are infinite when $n \in [1, 2)$ and finite when $n \geq 2$. However, the naked singularity is gravitationally strong only in the case when $n = 1$. When $n > 1$, it is gravitationally weak. Thus, we can conclude that the inertial forces which act on the particle when it escapes the singularity are finite only when the singularity is gravitationally weak and infinite when it is gravitationally strong. However, the weak naked singularity is not that interesting because the manifold can be extended through it. Thus, if we consider the black hole or the naked singularity formation in the case of Vaidya spacetime, one should consider the linear mass function $M(v) = \lambda v^n$, where λ is real positive constant. One should also note that only the linear mass function is the solution of the Einstein equation which violate CCC because it states that only the strong singularity must be always covered with horizon.

Conflict of Interest

The author declares that there is no conflict of interest, either existing or potential.

References

Dwivedi, I. H., Joshi, P. S. (1989) On the nature of naked singularities in Vaidya spacetimes. *Classical and Quantum Gravity*, 6 (11), artuicle 1599. https://doi.org/10.1088/0264-9381/6/11/013 (In English)

Landau, L. D., Lifshitz, E. M. (1980) *Course of theoretical physics series. Vol. 2. The classical theory of fields*. 4th ed. Oxford: Butterworth-Heinemann Publ., 444 p. (In English)

Nolan, B. C. (1999) Strengths of singularities in spherical symmetry. *Physical Review D*, 60 (2), article 024014. https://doi.org/10.1103/PhysRevD.60.024014 (In English)

Poisson, E. (2004) *A relativist's toolkit: The mathematics of black-hole mechanics*. Cambridge: Cambridge University Press, 233 p. (In English)

Tipler, F. J. (1977) Singularities in conformally flat spacetimes. *Physics Letters A*, 64 (1), 8–10. https://doi.org/10.1016/0375-9601(77)90508-4 (In English)

Vaidya, P. C., Raychaudhuri, A. K., Dadhich, N. (1985) *A random walk in relativity and cosmology: Essays in honour of P. C. Vaidya and A. K. Raychaudhuri*. New York: Wiley Publ., 236 p. (In English)

Physics of Semiconductors. Semiconductors

UDC 538.945.9

EDN NFNKXG
https://www.doi.org/10.33910/2687-153X-2022-3-2-86-99

Electronic defects in lattices of YBa_2Cu_3O7 and $La_{2-x}Sr_xCuO_4$

A. V. Marchenko[1], P. P. Seregin✉[1], V. S. Kiselev[1]

[1] Herzen State Pedagogical University of Russia, 48 Moika Emb., Saint Petersburg 191186, Russia

Authors

Alla V. Marchenko, ORCID: 0000-0002-9292-2541, e-mail: al7140@rambler.ru

Pavel P. Seregin, ORCID: 0000-0001-5004-2047, e-mail: ppseregin@mail.ru

Valentin S. Kiselev, e-mail: kiselev.valentin@gmail.com

For citation: Marchenko, A. V., Seregin, P. P., Kiselev, V. S. (2022) Electronic defects in lattices of $YBa_2Cu_3O_7$ and $La_{2-x}Sr_xCuO_4$. *Physics of Complex Systems*, 3 (2), 86–99. https://www.doi.org/10.33910/2687-153X-2022-3-2-86-99. EDN NFNKXG

Received 28 February 2022; reviewed 28 March 2022; accepted 28 March 2022.

Funding: The study did not receive any external funding.

Abstract. Using emission Mössbauer spectroscopy data for the ^{67}Zn isotope and nuclear quadrupole resonance data for the ^{17}O isotope, as well as calculations of the lattice electric field gradient, the effective charges of all atoms in superconducting copper metal oxide $YBa_2Cu_3O_7$ and $La_{2-x}Sr_xCuO_4$ crystal lattices were determined. The effective charges of metal atoms and most oxygen atoms correspond to their standard oxidation states (Y^{3+}, La^{3+}, Ba^{2+}, Sr^{2+}, Cu^{2+} and O^{2-}). However, the atoms of chain oxygen (in $YBa_2Cu_3O_7$) and planar oxygen (in $YBa_2Cu_3O_7$ and $La_{2-x}Sr_xCuO_4$) show a reduced charge, which is explained by the localisation of holes in the corresponding sublattices.

Keywords: Mössbauer spectroscopy, nuclear quadrupole resonance, electric field gradient tensor, atomic charges, high-temperature superconductors

Introduction

The discovery of the high-temperature superconductivity phenomenon in copper metal oxides (Bednorz, Muller 1986) resulted in a large number of studies of nuclear quadrupole interaction (NQI) in typical materials of this kind—$YBa_2Cu_3O_{7-x}$ and $La_{2-x}Sr_xCuO_4$—through nuclear quadrupole resonance (NQR) method with probe nuclei ^{17}O (Ishida et al. 1991; Takigawa et al. 1989), ^{63}Cu (Ohsugi et al. 1994; Pennington et al. 1989), ^{137}Ba (Shore et al. 1992), ^{139}La (Ohsugi 1995), as well as through absorption Mössbauer spectroscopy (MS) with probe nuclei ^{57}Fe, ^{119}Sn, ^{151}Eu, ^{155}Gd, ^{161}Dy, ^{166}Er, ^{169}Tm, ^{170}Yb (Masterov et al. 1995) and emission MS with probe nuclei $^{67}Cu(^{67}Zn)$ and $^{67}Ga(^{67}Zn)$ (Marchenko et al. 2018a; 2018b; Terukov et al. 2018). NQI tensor parameters (the quadrupole interaction constant and the asymmetry parameter) provide information on the spatial distribution of electronic defects in various sublattices within high-temperature superconductors (HTSC). This information makes it possible to determine the effective charges of their atoms, which, in turn, naturally limits the number of models that should be used in quantum mechanical calculations of HTSC electronic properties. A reliable method for finding the effective charges of atoms is to compare the calculated and the experimental parameters of the NQI tensor.

In crystal lattices with high chemical bond ionicity, which includes copper metal oxides $YBa_2Cu_3O_{7-x}$ and $La_{2-x}Sr_xCuO_4$, two sources of the electric field gradient (EFG) on probe nuclei can be distinguished: crystal lattice ions (lattice EFG) and nonspherical valence shells of the probe atoms (valence EFG). The total EFG on the probe nucleus is determined by the parameters (Marchenko et al. 2018a; 2018b)

$$U_{zz} = (1-\gamma)V_{zz} + (1-R_0)W_{zz}, \quad (1)$$

$$\eta = \frac{(1-\gamma)V_{zz}\eta_{lat} + (1-R_0)W_{zz}\eta_{val}}{U_{zz}}, \quad (2)$$

$$\eta = \frac{U_{xx}-U_{yy}}{U_{zz}}, \eta_{cr} = \frac{V_{xx}-V_{yy}}{V_{zz}}, \eta_{val} = \frac{W_{xx}-W_{yy}}{W_{zz}}, \quad (3)$$

where U_{ii}, V_{ii}, and W_{ii} are the components of the diagonalised total, lattice and valence EFG tensors, U_{zz}, V_{zz}, and W_{zz} are the principal components of these tensors, η, η_{lat}, η_{val} are the asymmetry parameters of these tensors, γ, R_0 are the Sternheimer coefficients, that should consider antiscreening and screening processes of the probe nucleus by the internal electron shells of the probe atom from external charges.

Blaha et al., suggested the full potential linearised-augmented-plane-wave (LAPW) method for the theoretical calculation of the parameters of the total EFG tensor using the local-density-approximation (LDA) (Blaha et al. 1985). This calculation is carried out without additional approximations such as the Sternheimer antishielding coefficients. Using this approach, EFG calculations "from first principles" based on LDA for high-temperature superconductors $YBa_2Cu_3O_7$ (Schwarz et al. 1990) were performed. When using the X-ray diffraction data (Beno et al. 1987) for $YBa_2Cu_3O_7$ and the nuclear quadrupole moment Q = –0.211 b for ^{63}Cu and Q = –0.026 b for ^{17}O while converting NQR frequencies to EFG, the calculated EFGs were in good agreement with the experimental NQR measurements with ^{63}Cu (Pennington et al. 1989), ^{17}O (Takigawa et al. 1989) and ^{137}Ba (Shore et al. 1992) for Ba, Cu, and O sites, with the exception of the planar copper Cu(2) nodes, where the main component of the experimental EFG tensor is more than twice the calculated value. Similar results were also presented in (Yu et al. 1991). In connection with this discrepancy, the authors of (Ambrosch-Draxl et al. 1991) reported on EFG calculations for $YBa_2Cu_3O_7$, in which the ambiguities presented in LAPW were eliminated. Despite the changes in the calculations, the calculated EFG at the Cu(2) site is similar to the values obtained in earlier LAPW studies. This means that the discrepancy between the EFG calculated within the LDA framework and the experimental one cannot be explained by a computational artefact and confirms the assumption made in (Schwarz et al. 1990), that the discrepancy is a real LDA error. It is emphasised that the EFG tensor components are only the second derivatives of the Coulomb potential and thus represent well-defined properties of the ground state, uniquely determined by the charge density.

It can be noted here that the studies of $La_{2-x}Sr_xCuO_4$ performed in (Sun et al. 2015; 2016) demonstrate how the doping electronic structures of high-temperature cuprate superconductors can be accurately modelled based on the first principles developed in (Lee et al. 2021). These calculations correctly predict the key experimentally observed features of the electronic structure and magnetism of $La_{2-x}Sr_xCuO_4$ without involving any free parameters. Thus, studies (Lee et al. 2021; Sun et al. 2016) open a new way to investigate the first principles of electronic structures and broader properties of correlated materials in general.

It is possible to just compare the theoretical and experimental parameters of the lattice EFG tensor to determine the effective charges of atoms (Marchenko et al. 2018a; 2018b; Terukov et al. 2018). If the electron shells of the probe atom are completely (or half) filled, then the electron cloud can be considered as consisting of several concentric spheres. The strength of the electrostatic field from such spheres on the nucleus is zero, so only the charges of the neighbouring atoms should be taken into consideration when calculating the EFG at the nucleus of an atom-probe (lattice probe).

The method of making lattice EFG tensor calculations using the point charge model is quite simple and clear. For such a calculation, only the unit cell parameters are required, which are known for most HTSCs from X-ray diffraction studies. The term "effective charges" refers to the charges that are required to describe the electric field of ions using the Coulomb potential. Effective charges accurately present the valence states of ions at the lattice sites and the significant deviations from their standard valence states (Seregin, Masterov, Nasredinov 1992; Seregin, Marchenko, Seregin et al. 1992; 2015). Such calculations for the $YBa_2Cu_3O_7$ and $La_{2-x}Sr_xCuO_4$ lattices have been carried out in many works (see, for example, (Adrian 1989; Garcia, Bennemann 1989; Lyubutin et al. 1989; Seregin et al. 1992; 2015; Shimizu 1993)), but their results are in poor agreement with experimental data (Ishida et al. 1991; Masterov et al. 1995; Ohsugi 1995; Ohsugi et al. 1994; Pennington et al. 1989; Shore et al. 1992; Takigawa et al. 1989).

This is explained by the fact that copper metal oxides $YBa_2Cu_3O_7$ and $La_{2-x}Sr_xCuO_4$ predominantly contain atoms that do not form lattice probes.

This study describes effective charge determination for atoms in the copper metal oxides $YBa_2Cu_3O_7$ and $La_{2-x}Sr_xCuO_4$. The calculated EFG tensor parameters are compared with the experimental NQI tensor parameters measured by NMR/NQR or MS using the lattice probes located at the lattice sites. The EFG tensor parameters are the main components of the lattice EFG tensors at the *i*-sites of the lattice V_{zzi} and the asymmetry parameters of these tensors η_{lati}. The parameters of the NQI tensors are the quadrupole interaction constants $C_{expi} = Q_i(1 - \gamma_i)V_{zzi} = \alpha_i V_{zzi}$ and the asymmetry parameters η_{expi} (here $\alpha_i = Q_i(1 - \gamma_i)$ is the electron-nuclear parameter of the lattice *i*-probe located at the *i*-site of the lattice, γ_i is the Sternheimer coefficient of the *i*-probe and Q_i is the quadrupole moment of the atomic nucleus of the *i*-probe).

Requirements for lattice probes

There are several requirements for the lattice probes (Seregin et al. 2015):

- it is necessary to use such probes that their position in the lattice is known a priori;
- the possibility of uncontrolled appearance of point defects in the lattice (such as vacancies or atoms displaced into interstitial spaces) is excluded during probe introduction. Such defects distort the results of EFG tensor calculations;
- to eliminate any uncertainties in the theoretical values of nucleus quadrupole moments and Sternheimer coefficients, as well as to determine the effective charges of atoms in units of electron charge, it is necessary to experimentally determine the coefficient $\alpha = eQ(1 - \gamma)$ for at least one probe that is used;
- to reduce the influence that coefficient α uncertainties have on the values of the obtained effective charges, it is appropriate to use the minimum number of probes and, in the ideal case, use one probe each in the cationic and anionic sublattices (of course, each probe should replace as many crystallographically nonequivalent sites of the crystal lattice as possible);
- for crystals containing one lattice probe in two crystallographically non-equivalent positions, one should not compare the values V_{zzi} and $C_{expi} = eQ_i(1 - \gamma_i)V_{zzi}$, but the values of the ratios V_{zz1}/V_{zz2} and C_{exp1}/C_{exp2}, where V_{zz1}, V_{zz2} are the principal components of the lattice EFG tensor at structurally nonequivalent sites 1 and 2 occupied by the lattice probe atom, and C_{exp1} and C_{exp2} are the quadrupole interaction constants for the lattice probe at these sites (i.e., it is proposed to exclude quadrupole moments of probe nuclei and Sternheimer coefficients of probe atoms);
- All of these conditions for $YBa_2Cu_3O_7$ and $La_{2-x}Sr_xCuO_4$ are satisfied for the $^{67}Zn^{2+}$ probe using emission MS (Seregin et al. 2015);
- when using emission MS with $^{67}Cu(^{67}Zn)$ isotopes, copper atoms form a lattice probe of divalent zinc $^{67}Zn^{2+}$ after beta decay of ^{67}Cu at the sites of divalent copper Cu^{2+} in the $YBa_2Cu_3O_7$ and $La_{2-x}Sr_xCuO_4$ lattices;
- when using emission MS with $^{67}Ga(^{67}Zn)$ isotopes, trivalent gallium atoms $^{67}Ga^{3+}$ replace trivalent yttrium atoms Y^{3+} in the $YBa_2Cu_3O_7$ lattice or trivalent lanthanum atoms La^{3+} in the $La_{2-x}Sr_xCuO_4$ lattice, and the lattice probe of bivalent zinc $^{67}Zn^{2+}$ stabilises at trivalent yttrium (or trivalent lanthanum) sites after the electron capture in ^{67}Ga.

The results of Mössbauer spectroscopy of the $YBa_2Cu_3O_7$ compound (Seregin et al. 2015) show that in some structural positions the oxygen atom can be considered a $^{17}O^{2-}$ lattice probe, making it possible to determine the effective charges of all atoms in the $YBa_2Cu_3O_7$ and $La_{2-x}Sr_xCuO_4$ crystal lattices using the NQR data with the ^{17}O isotope (Masterov et al. 1995; Terukov et al. 2018).

To confirm the validity of the effective charges determined in $La_{2-x}Sr_xCuO_4$, other lattice probes can also be introduced:

- when using emission MS with $^{57}Co(^{57m}Fe)$ isotopes, the atoms of bivalent cobalt Co^{2+} replace the atoms of bivalent copper Cu^{2+} in the $La_{2-x}Sr_xCuO_4$ lattice, and the lattice probe of trivalent iron $^{57m}Fe^{3+}$ is stabilised at the sites of bivalent copper after electron capture in ^{57}Co;
- when using emission MS with $^{155}Eu(^{155}Gd)$ isotopes, the trivalent europium atoms $^{155}Eu^{3+}$ replace the atoms of trivalent lanthanum La^{3+} in the $La_{2-x}Sr_xCuO_4$ lattice, and the lattice probe of trivalent gadolinium $^{155}Gd^{3+}$ is stabilised at the sites of trivalent lanthanum after the decay of ^{155}Eu.

 https://www.doi.org/10.33910/2687-153X-2022-3-2-86-99

Experimental techniques

EFG tensors calculations

Copper oxide Cu_2O and superconducting $YBa_2Cu_3O_7$ and $La_{2-x}Sr_xCuO_4$ ceramics were chosen as objects of study.

The Cu_2O compound crystallises in a cubic lattice (Wells 1984). The $YBa_2Cu_3O_7$ compound has an orthorhombic structure (see Fig. 1a) (Yvon, Francois 1989). The $La_{2-x}Sr_xCuO_4$ solid solutions crystallise in a lattice of the K_2NiF_4 type (a weakly distorted orthogonal structure; for $x > 0.1$, the lattice becomes tetragonal (see Fig. 1b) (Yvon, Francois 1989).

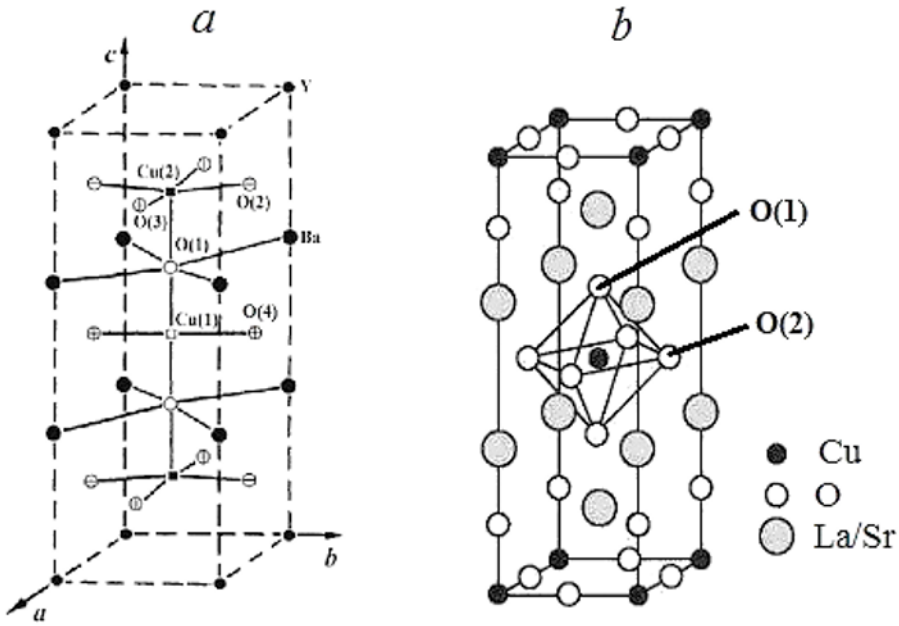

Fig. 1. Unit cells of $YBa_2Cu_3O_7$ (a) and $La_{2-x}Sr_xCuO_4$ (b)

The components of the lattice EFG tensor were calculated using the point-charge model with the relations (Seregin et al. 2015).

$$V_{\alpha\alpha} = \sum_k e_k \sum_i \frac{1}{r_{ki}^3}\left[\frac{3\alpha_{ki}^2}{r_{ki}^2} - 1\right] = \sum_k e_k G_{\alpha\alpha k},$$
$$V_{\alpha\beta} = \sum_k e_k \sum_i \frac{3\alpha_{ki}\beta_{ki}}{r_{ki}^5} = \sum_k e_k G_{\alpha\beta k} \qquad (4)$$

where k is the summation index over sublattices, i is the summation index over sublattice sites, α, β are the Cartesian coordinates, e_k are the effective charges of atoms of the k-sublattice (in units of the electron charge e), r_{ki} is the distance from the i-ion of the k-sublattice to node where the EFG is calculated.

The lattice of the Cu_2O compound was represented as Cu_4O_2, and the atomic coordinates c and unit cell parameters were set according to (Wells 1984).

According to (Yvon, Francois 1989), a unit cell of the $YBa_2Cu_3O_7$ compound contains nodes of yttrium, barium, chain copper Cu(1), planar copper Cu(2), apical oxygen O(1), planar oxygen O(2), O(3) and chain O(4) oxygen (see Fig. 1a). The $YBa_2Cu_3O_7$ lattice was represented as $YBa_2Cu(1)Cu(2)_2O(1)_2O(2)_2O(3)_2O(4)$, and the summation index over sublattices in the formula (3) took the following values:

k =	1	2	3	4	5	6	7	8
atom	Y	Ba	Cu(1)	Cu(2)	O(1)	O(2)	O(3)	O(4)

According to (Yvon, Francois 1989), a unit cell of $La_{2-x}Sr_xCuO_4$ solid solution contains nodes of lanthanum (strontium), copper, apical O(1) and planar oxygen O(2) (see Fig. 1b). The $La_{2-x}Sr_xCuO_4$ lattice was represented as in the form $(La,Sr)_2CuO(l)_2O(2)_2$, with the crystallographic parameters taken from (Yvon, Francois 1989; Tarascon et al. 1987); the summation index over sublattices in the formula (3) took the following values:

k =	1	2	3	4	5
atom	La	Sr	Cu	O(1)	O(2)

The tensors $G_{\alpha\alpha}$ and $G_{\beta\beta}$ were calculated inside spheres with a radius of 30 Å, and the obtained parameters of the tensors are consistent with the literature data (Seregin et al. 2015).

Sample synthesis and Mössbauer spectra measurement

Cu_2O copper oxide was obtained by calcining CuO in vacuum. $YBa_2Cu_3O_7$ and $La_{2-x}Sr_xCuO_4$ compounds ($x = 0 \div 1$) were prepared using ceramic technology (Seregin et al. 2015). The $YBa_2Cu_3O_7$ samples had an orthorhombic structure, while the $La_{2-x}Sr_xCuO_4$ samples had a K_2NiF_4 type structure. The obtained materials were single-phase with superconducting transition temperatures of 91 K for $YBa_2Cu_3O_7$ and 25, 37, 32 K for $La_{2-x}Sr_xCuO_4$ (where x = 0.1, 0.15, 0.2). Ceramics were alloyed with isotopes ^{67}Cu, ^{67}Ga, ^{57}Co and ^{155}Eu during diffusion annealing (Seregin et al. 2015).

Mössbauer spectra were recorded at 80 K (^{57}Co, ^{155}Eu) and 4.2 K (^{67}Cu, ^{67}Ga) with $K_4{}^{57}Fe(CN)_6.3H_2O$, $^{155}GdPd_3$, and ^{67}ZnS absorbers.

Table 1. Experimental NQI parameters at the lattice sites of $YBa_2Cu_3O_7$, $La_{1.85}Sr_{0.15}CuO_4$, and Cu_2O

Compound	Node	Probe	Method	C_{exp},MHz	η_{exp}	z-axis of the EFG tensor	Reference
$YBa_2Cu_3O_7$	Y	^{67}Zn	MS $^{67}Ga(^{67}Zn)$	−2.2(3)	0.8(1)	c	[*]
	Ba	^{137}Ba	NQR ^{137}Ba	|56.4(1)|	0.94(2)	c	[6]
	Cu(1)	^{67}Zn	MS $^{67}Cu(^{67}Zn)$	+20.1(3)	0.95(3)		[*]
	Cu(2)	^{67}Zn	MS $^{67}Cu(^{67}Zn)$	+11.8(3)	≤ 0.2		[*]
	O(1)	^{17}O	NMR ^{17}O	|7.3(1)|	0.32(2)	c	[2]
	O(2)	^{17}O	NMR ^{17}O	|6.4(1)|	0.24(2)	b	[2]
	O(3)	^{17}O	NMR ^{17}O	|6.6(1)|	0.21(2)	a	[2]
	O(4)	^{17}O	NMR ^{17}O	|10.9(1)|	0.41(2)	b	[2]
$La_{1.85}Sr_{0.15}CuO_4$	La,Sr	^{67}Zn	MS $^{67}Cu(^{67}Zn)$	−2.7(2)	≤ 0.2		[*]
	Cu	^{67}Zn	MS $^{67}Cu(^{67}Zn)$	11.4(5)	≤ 0.2		[*]
	O(1)	^{17}O	NMR ^{17}O	|1.33(5)|	0.0		[3]
	O(2)	^{17}O	NMR ^{17}O	|4.6(1)|	0.36(2)		[3]
Cu_2O	Cu	^{67}Zn	MS $^{67}Cu(^{67}Zn)$	−22.0(3)	≤ 0.2		[*]

[*]—the results of this work.

https://www.doi.org/10.33910/2687-153X-2022-3-2-86-99

Experimental results and discussion

MS data

The Mössbauer spectra of ^{67}Zn are shown in Figs. 2–4, the results of their processing are summarised in Table 1. The same table shows NQR data for barium (Shore et al. 1992) and oxygen (Ishida et al. 1991; Takigawa et al. 1989) sites.

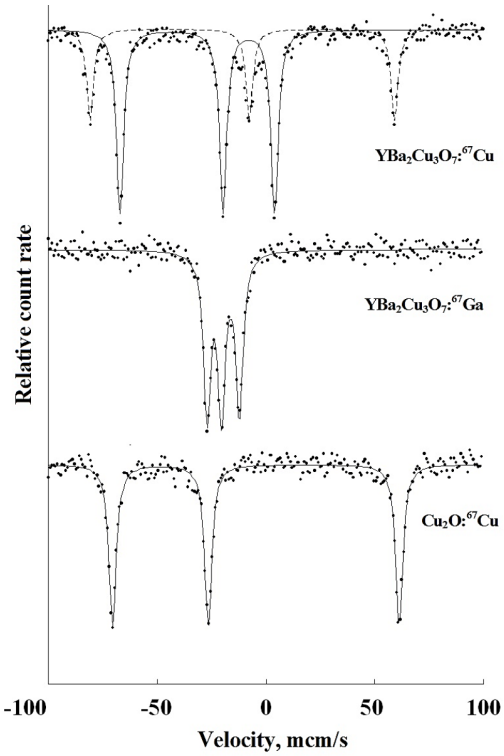

Fig. 2. ^{67}Cu(^{67}Zn) and ^{67}Ga(^{67}Zn) Mössbauer spectra of $YBa_2Cu_3O_7$ and Cu_2O compounds at 4.2 K

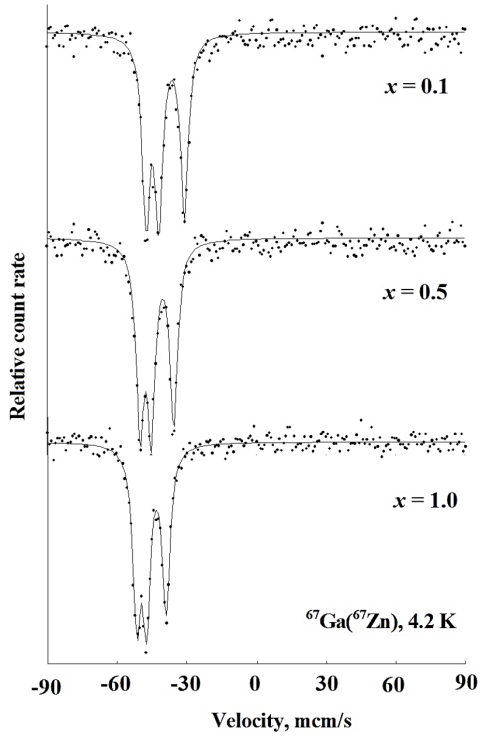

Fig. 3. ^{67}Cu(^{67}Zn) Mössbauer spectra of $La_{2-x}Sr_xCuO_4$ solid solutions for x = 0.1, 0.5, and 1.0 at 4.2 K

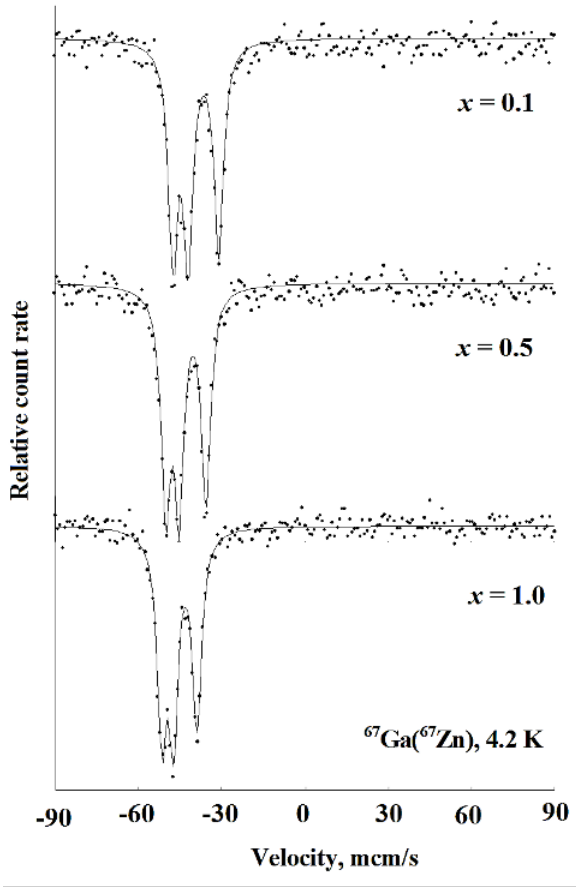

Fig. 4. ^{67}Ga(^{67}Zn) Mössbauer spectra of $La_{2-x}Sr_xCuO_4$ solid solutions for x = 0.1, 0.5, and 1.0 at 4.2 K

The Mössbauer emission spectra of ^{67}Cu(^{67}Zn) and ^{67}Ga(^{67}Zn) of all studied materials are either well-resolved quadrupole triplets (spectra of Cu_2O:^{67}Cu, $YBa_2Cu_3O_7$:^{67}Ga (see Fig. 2), $La_{2-x}Sr_xCuO_4$:^{67}Cu (see Fig. 3), and $_{2-x}Sr_xCuO_4$:^{67}Ga (see Fig. 4)), or a superposition of two quadrupole triplets ($YBa_2Cu_3O_7$:^{67}Cu spectrum (see Fig. 2)). According to the values of isomer shifts, these spectra correspond to the lattice centres of divalent zinc $^{67}Zn^{2+}$ either at copper sites (^{67}Cu(^{67}Zn) spectra) or at yttrium and lanthanum sites (^{67}Ga(^{67}Zn) spectra). The number of quadrupole triplets in the experimental spectra is determined by the number of crystallographic positions occupied by the substituting atoms.

The ^{57}Co(^{57m}Fe) and ^{155}Eu(^{155}Gd) Mössbauer emission spectra of $La_{2-x}Sr_xCuO_4$ solid solutions are quadrupole triplets (see Figs. 5 and 6). According to the values of isomeric shifts, these spectra correspond to the lattice centres of trivalent iron $^{57m}Fe^{3+}$ and trivalent gadolinium $^{155}Gd^{3+}$ at lanthanum sites.

The noncubic symmetry of the local environment of copper, yttrium, and lanthanum atoms leads to the splitting of the spectra into quadrupole triplets (^{67}Cu(^{67}Zn) and ^{67}Ga(^{67}Zn) spectra) or quadrupole doublets (^{57}Co(^{57m}Fe) and ^{155}Eu(^{155}Gd) spectra).

https://www.doi.org/10.33910/2687-153X-2022-3-2-86-99

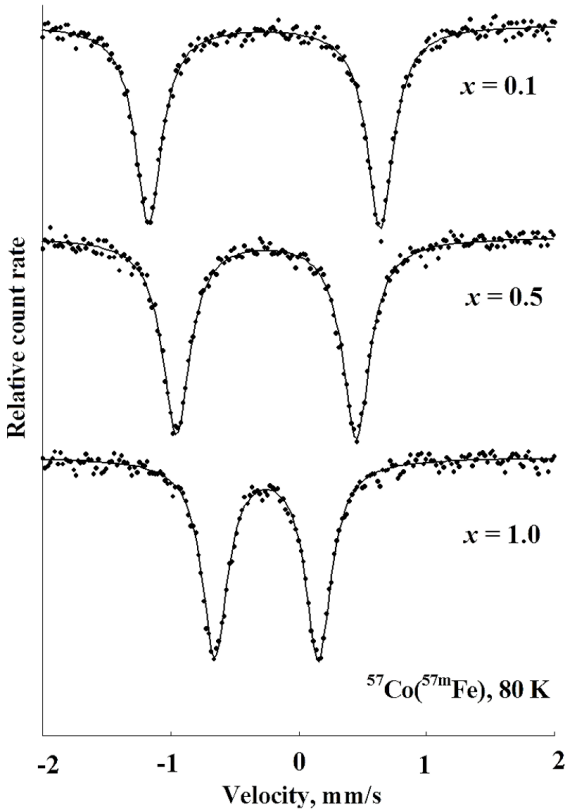

Fig. 5. ^{57}Co(^{57m}Fe) Mössbauer spectra of $La_{2-x}Sr_xCuO_4$:^{57}Co for x = 0.1, 0.5, and 1.0 at 80 K

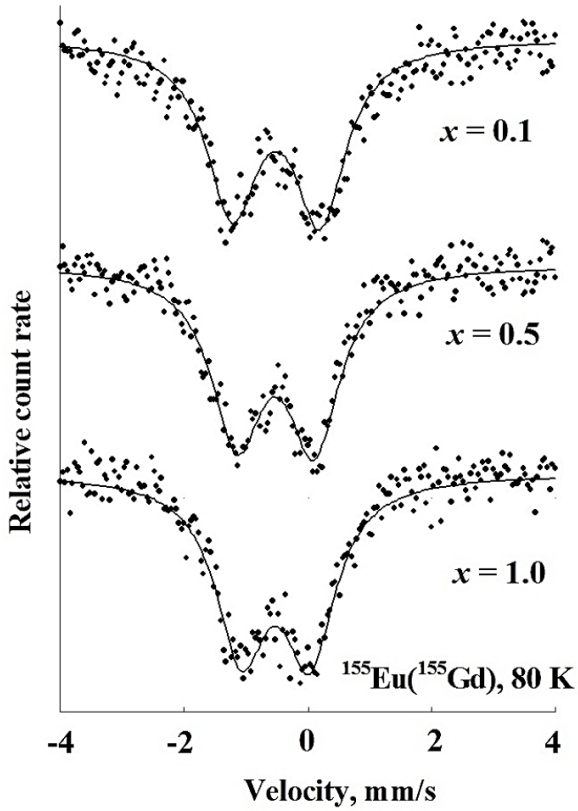

Fig. 6. ^{155}Gd Mössbauer spectra of $La_{2-x}Sr_xCuO_4$:^{155}Eu solid solutions for x = 0.1, 0.5, and 1.0 at 80 K

Determining the $\alpha_{Zn} = eQ_{Zn}(1 - \gamma_{Zn})$ coefficient for the $^{67}Zn^{2+}$ probe

For the $Cu^{+}_{2}O^{2-}$ model, the calculation for copper sites yields $V_{zz} = -1.093$ e/Å^3, which leads to α_{Zn} equal to 20.1(3) MHz.Å^3/e for ^{67}Zn=– centres at copper sites in the Cu_2O lattice.

Determining effective atom charges in the $YBa_2Cu_3O_7$ lattice

To determine the effective charges of $YBa_2Cu_3O_7$ lattice atoms, emission MS data on the isotopes ^{67}Cu(^{67}Zn) and ^{67}Ga(^{67}Zn) and NQR data on the isotope ^{17}O were used (Takigawa et al. 1989).

A system of equations was compiled, including

- the equation of electroneutrality:

$$e_1 + 2e_2 + e_3 + 2e_4 + 2e_5 + 2e_6 + 2e_7 + e_8 = 0, \quad (5)$$

- the equation relating the quantities V_{zz1}. and C_1 for the $^{67}Zn^{2+}$ probe at yttrium nodes:

$$\alpha_{Zn} \sum_{k=1}^{k=8} e_k G_{zzk1} = C_1, \quad (6)$$

- the equation relating the quantities V_{zz3}/V_{zz4} and $P_{34} = C_3/C_4$ for the $^{67}Zn^{2+}$ probe at the Cu(1) and Cu(2) sites:

$$\sum_{k=1}^{k=8} e_k \left[G_{zzk3} - P_{34} G_{zzk4} \right] = 0, \quad (7)$$

- equation relating the values V_{zz5}/V_{zz6} and $P_{56} = C_5/C_6$ for the $^{17}O^{2-}$ probe at the O(5) and O(7) nodes:

$$\sum_{k=1}^{k=8} e_k \left[G_{zzk5} - P_{56} G_{zzk6} \right] = 0, \quad (8)$$

- four equations relating the calculated and experimental values of the asymmetry parameters of the EFG tensors for the $^{67}Zn^{2+}$ probe at the copper sites and for the $^{17}O^{2-}$ probe at the O(1) and O(2) sites:

$$\sum_{k=1}^{k=8} e_k \left[G_{xxkl} - G_{yykl} - \eta_l G_{zzkl} \right] = 0, \quad (9)$$

where l = 3, 4, 5, 6.

Additional factors that were taken into account are as follows:

- the principal axes of the EFG tensors for the $^{17}O^{2-}$ centres at the O(1) and O(2) sites coincide with the crystallographic axes *c* and *b*, respectively (Takigawa et al. 1989);
- the main axis of the EFG tensor for $^{137}Ba^{2+}$ centres is directed along the crystallographic *c* axis (Shore et al. 1992);
- the main axis of the EFG tensor for $^{155}Gd^{3+}$ centres at Y sites is directed along the crystallographic *c* axis (Wortmann et al. 1989);
- solutions with negative charges of cations or positive charges of anions were rejected as having no physical meaning.

The accuracy of effective charge e_k values obtained from the system of equations (5–9) is limited by the assumption that there is no valence electric field on probe nuclei. As an example, Table 2 shows the atom charges obtained using the experimental values from Table 1 and various structural data (Capponi et al. 1987; Francois et al. 1988; Konstatntinovic et al. 1989; Le Page et al. 1987; Yvon, Francois 1989). The reduced values of the O(4) and O(3) charges reflect charge distribution in the $YBa_2Cu_3O_7$ lattice,

 https://www.doi.org/10.33910/2687-153X-2022-3-2-86-99

while the deviations of remaining atoms' charges from the standard oxidation states are random and are associated with the difference in the temperatures for determining the NQI parameters and the parameters of the $YBa_2Cu_3O_7$ crystal lattice structure, and also with the errors in the latter.

Table 2. Effective charges of atoms of the $YBa_2Cu_3O_7$ lattice obtained by solving the system of equations (5–9) with different structural data at different temperatures

Structural data	T, K	e1	e2	e3	e4	e5	e6	e7	e8	Model
[28]	5 K	2.92	2.04	1.96	2.00	–2.09	–1.93	–1.81	–1.28	1
[28]	320 K	2.80	1.90	1.88	1.92	–1.99	–1.83	–1.71	–1.22	2
[29]	5 K	2.91	2.01	1.88	1.99	–2.05	–1.92	–1.80	–1.25	3
[31]	298 K	3.03	2.06	2.13	2.14	–2.18	–2.00	–1.91	–1.36	4
[30]	9 K	2.99	2.00	2.01	2.00	–2.00	–2.00	–1.80	–1.40	5
[25]	295K	3.00	1.99	2.00	2.01	–2.00	–2.00	–1.85	–1.30	6

The models given in Table 2 satisfy the assumption made in (Baryshev et al. 2011; Mitsen, Ivanenko 2007) about the localisation of holes in $YBa_2Cu_3O_{7-x}$ around Cu ions in CuO_3 chains on oxygen ions (O(4) crystallographic position).

For all models from Table 2, the calculated parameters of the lattice EFG tensors with different structural data turn out to be similar. For model 6, these values are shown in Table 3.

Table 3. Components of lattice EFG tensors for $YBa_2Cu_3O_7$ crystal sites (model 6)

Node	Vaa, e/Å3	Vbb, e/Å3	Vcc, e/Å3	ηlat
Y	0.006	0.107	– 0.113	0.89
Ba	– 0.118	– 0.003	0.121	0.94
Cu(1)	0.982	– 0.036	– 0.946	0.97
Cu(2)	– 0.263	– 0.324	0.587	0.10
O(1)	– 0.158	– 0.331	0.489	0.35
O(2)	– 0.153	0.385	– 0.232	0.21
O(3)	0.439	– 0.206	– 0.233	0.06
O(4)	– 0.086	0.575	– 0.489	0.70

The obtained parameters of the lattice EFG tensors can be used to interpret NQR data on the ^{137}Ba isotope, for which the value C_{exp} = 56.4MHz, η_{exp} = 0.94 was found in $YBa_2Cu_3O_7$ (Shore et al. 1992). We calculated the lattice EFG tensor at Ba nodes for model 6 in Table 3. For the $^{137}Ba^{2+}$ probe, the value $\alpha_{Ba} = e\,Q\,(1-\gamma)$ = 470(9) MHz.e/Å^3 was obtained.

Similarly, the value $\alpha_O = e\,Q\,(1-\gamma)$ can be determined for lattice centres $^{17}O^{2-}$. Using the values V_{zz5} (see Table 3) and C_5 (see Table 1) for the $^{17}O^{2-}$ centers at the nodes O(1) of the $YBa_2Cu_3O_7$ lattice, we obtained α_O = 14.9(2) MHz.Å^3/e.

Finally, we obtained $z \,||\, c$ and $U_{zz} < 0$ for the $^{155}Gd^{3+}$ lattice probe in the $YBa_2Cu_3O_7$ compound within the framework of the point charge model (see Table 3). This is in agreement with MS results (Wortmann et al. 1989) obtained on the ^{155}Gd isotope for the compound $GdBa_2Cu_3O_7$.

Effective atom charges in the lattices of $La_{2-x}Sr_xCuO_4$ solid solutions

To determine the effective atom charges in the $La_{2-x}Sr_xCuO_4$ lattice, we used emission MS data on the ^{67}Cu(^{67}Zn) and ^{67}Ga(^{67}Zn) isotopes, as well as NQR data on the ^{17}O isotope (Ishida et al. 1991). It should be noted that according to the data on the ^{17}O isotope, the asymmetry parameter of the EFG tensor for planar oxygen O(2) lattice $La_{1.85}Sr_{0.15}CuO_4$ is different from zero (see Table 1), whereas according to the calculations of the lattice EFG tensor for this oxygen, η_4 = 0. In other words, the crystal probe can only be the apical oxygen centre O(1).

Thus, the following system of equations was compiled:

- the equation of electroneutrality:

$$2e_1 + e_2 + 2e_3 + 2e_4 = 0, \quad (10)$$

- the equation relating the quantities V_{zz1}. and C_1 for the $^{67}Zn^{2+}$ probe at lanthanum nodes:

$$\alpha_{Zn} \sum_{k=1}^{k=4} e_k G_{zzk1} = C_1, \quad (11)$$

- the equation relating the quantities V_{zz2}. and C_2 for the $^{67}Zn^{2+}$ probe at copper nodes;

$$\alpha_{Zn} \sum_{k=1}^{k=4} e_k G_{zzk2} = 0, \quad (12)$$

where α_{Zn} = 20.1(3) MHz.Å^3/e.

- the equation relating the quantities V_{zz3}. and C_3 for the $^{17}O^{2-}$ probe at O(1) nodes;

$$\alpha_{\text{î}} \sum_{k=1}^{k=4} e_k G_{zzk3} = 0, \quad (13)$$

where α_O = 14.9(2) MHz.Å^3/e.

The effective charges of metal atoms and apical oxygen atoms of the $La_{2-x}Sr_xCuO_4$ lattice, as in the case of the $YBa_2Cu_3O_7$ lattice, correspond to the standard oxidation states of these atoms. However, for planar oxygen atoms, a reduced charge of planar oxygen atoms is observed, which is consistent with the authors' assumption (Baryshev et al. 2011; Mitsen, Ivanenko 2007) about the localisation of a hole in the energy zone formed by the electronic states of O(2) atoms. Taking into account the error in determining the parameters of the lattice GAP tensors, the distribution of atomic charges in the $La_{2-x}Sr_xCuO_4$ lattice can be represented as

$$(La_{1.85}Sr_{0.15})^{2.925+}Cu^{2+}O(1)^{2-}{}_2(2)^{1.925-}{}_2. \quad (13)$$

To confirm the model (13), we performed a co-representation of the calculated $P(x) = [V_{zz}]_x/[V_{zz}]_{x=0.1}$ and experimental $P_{exp} = [eQU_{zz}]_x/[eQU_{zz}]_{x=0.1}$ dependencies in lanthanum nodes (see Fig. 7) and copper (see Fig. 8) lattices of $La_{2-x}Sr_xCuO_4$ solid solutions. MS was used on isotopes $^{57}Co(^{57m}Fe)$, $^{67}Cu(^{67}Zn)$ (see Fig. 7) and $^{67}Ga(^{67}Zn)$, $^{155}Eu(^{155}Gd)$ (see Fig. 8). The indicated permutations were carried out for four models of hole localisation: the hole is located in the sublattice of copper; in the sublattice of apical oxygen; in the sublattice of planar oxygen and the hole is distributed between sublattices of apical and planar oxygen. The dependences of P(x) in Figs. 7 and 8 can be explained if the hole is localised mainly in the positions of planar oxygen.

Conclusion

Using only crystallographic data, Mossbauer spectroscopy data on the ^{67}Zn isotope and nuclear quadrupole resonance on the ^{17}O isotope, as well as calculations of lattice EFG tensors, the effective charges of all atoms of superconducting copper metal oxide $YBa_2Cu_3O_7$ and $La_{2-x}Sr_xCuO_4$ lattices were determined. These charges correspond to the standard degrees of atom oxidation, with the exception of the chain and planar oxygen atoms in the $YBa_2Cu_3O_7$ lattice and planar oxygen atoms in the $La_{2-x}Sr_xCuO_4$ lattice. The reduced charge of these atoms is explained by the localisation of holes in the corresponding sublattices.

 https://www.doi.org/10.33910/2687-153X-2022-3-2-86-99

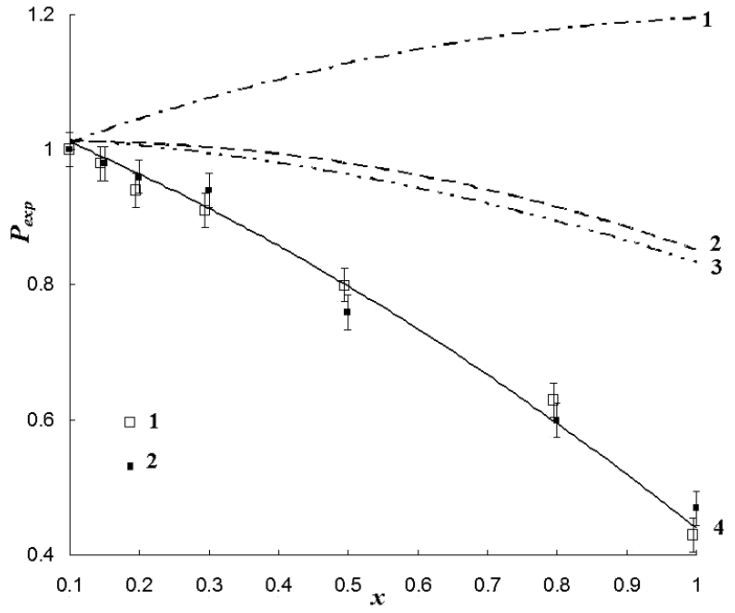

Fig. 7. Dependences of P_{exp} on x for $La_{2-x}Sr_xCuO_4$ for copper sites: (1) the hole is located in the copper sublattice; (2) the hole is in the O(1) sublattice; (3) the hole is in the O(2) sublattice; (4) the hole is distributed between the O(1) and O(2) sublattices; open and filled squares are experimental MS data with the $^{57}Co(^{57m}Fe)$ (1) and $^{67}Cu(^{67}Zn)$ (2) isotopes

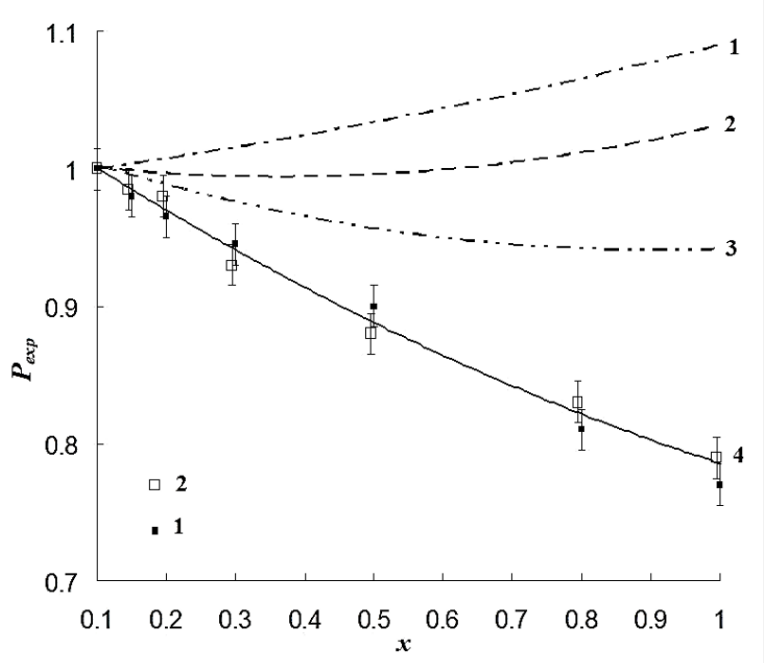

Fig. 8. Dependences of P_{exp} on x for $La_{2-x}Sr_xCuO_4$ for lanthanum sites: 1—the hole is localised in Cu positions; 2—the hole is localised in positions O(1); 3—the hole is localised in positions O(2); 4—the hole is localised in positions O(1) and O(2); open and filled squares are experimental data with the $^{67}Ga(^{67}Zn)$ (1) and $^{155}Eu(^{155}Gd)$ (2) isotopes

Conflict of Interest

The authors declare that there is no conflict of interest, either existing or potential.

References

Adrian, F. J. (1989) Structural implications of nuclear electric quadrupole splittings in high-T_c superconductors. *Physical Review B*, 38 (4), 2426–2431. https://doi.org/10.1103/physrevb.38.2426 (In English)

Ambrosch-Draxl, C., Blaha, P., Schwarz, K. (1991) Electronic structure and electric-field gradients for $YBa_2Cu_4O_8$ from density-functional calculations. *Physical Review B*, 44 (10), 5141–5147. https://doi.org/10.1103/physrevb.44.5141 (In English)

Baryshev, S. V., Kapustin, A. I., Bobyl, A. V. et al. (2011) Temperature dependences of $YBa_2Cu_3O_x$ and $La_{2-x}Sr_xCuO_4$ resistivity in terms of the negative-U centers model. *Superconductor Science and Technology*, 24, article 075026. https://doi.org/10.1088/0953-2048/24/7/075026 (In English)

Bednorz, J. G., Muller, K. A. (1986) Possible high T_c superconductivity in the Ba–La–Cu–O system. *Zeitschrift für Physik B Condensed Matter*, 64, 189–193. https://doi.org/10.1007/BF01303701 (In English)

Beno, M. A., Soderholm, L., Capone, D. W. et al. (1987) Structure of the single-phase high-temperature superconductor $YBa_2Cu_3O_{7-\delta}$. *Applied Physics Letters*, 51 (1), 57–60. https://doi.org/10.1063/1.98886 (In English)

Blaha, P., Schwarz, K., Herzig, P. (1985) First-principles calculation of the electric field gradient of Li_3N. *Physical Review Letters*, 54 (11), 1192–1198. https://doi.org/10.1103/PhysRevLett.54.1192 (In English)

Capponi, J. J., Chaillout, C., Hewat, A. W. et al. (1987) Structure of the 100 K superconductor $Ba_2YCu_3O_7$ between (5–300) K by neutron powder diffraction. *Europhysics Letters*, 3 (12), 1301–1307. https://doi.org/10.1209/0295-5075/3/12/009 (In English)

Francois, M., Junod, A., Yvon, K. et al. (1988) A study of the Cu-O chains in the high T_c superconductor $YBa_2Cu_3O_7$ by high resolution neutron powder diffraction. *Solid State Communications*, 66 (10), 1117–1125. https://doi.org/10.1016/0038-1098(88)90335-3 (In English)

Garcia, M. E., Bennemann, K. H. (1989) Theoretical study of the structural dependence of nuclear quadrupole frequencies in high-T_c superconductors. *Physical Review B*, 40 (13), 8809–8813. https://doi.org/10.1103/PhysRevB.40.8809 (In English)

Ishida, K., Kitaoka, Y., Zheng, G., Asayama, K. (1991) ^{17}O and ^{63}Cu NMR Investigations of high-T_c superconductor $La_{1.85}Sr_{0.15}CuO_4$ with T_c = 38 K. *Journal of the Physical Society of Japan*, 60 (10), 3516–3524. https://doi.org/10.1143/JPSJ.60.3516 (In English)

Konstatntinovic, J., Parette, G., Djordjevic, Z., Menelle, A. (1989) Structural transformations of the $YBa_2Cu_3O_{6.84}$ crystal lattice in the temperatute interval 9 K to 300 K. *Solid State Communications*, 70 (2), 163–166. https://doi.org/10.1016/0038-1098(89)90967-8 (In English)

Lee, C. C., Chiu, J.-Y., Yamada-Takamura, Y. et al. (2021) Hidden competing phase revealed by first-principles calculations of phonon instability in the nearly optimally doped cuprate $La_{1.875}Sr_{0.125}CuO_4$. *Physical Review B*, 104 (6), article 064114. https://doi.org/10.1103/PhysRevB.104.064114 (In English)

Le Page, Y., Siegrist, T., Sunshine, S. A. et al. (1987) Structural properties of $Ba_2YCu_3O_7$ high-T_c superconductors. *Physical Review B*, 36 (7), 3617–3621. https://doi.org/10.1103/PhysRevB.36.3617 (In English)

Lyubutin, I. S., Terziev, V. G., Dmitrieva, T. V., Gor'kov, V. P. (1989) Lattice sum calculations and electric field gradients for orthorhombic and tetragonal phases of $YBa_2Cu_3O_x$. *Physics Letters A*, 137 (3), 144–148. https://doi.org/10.1016/0375-9601(89)90101-1 (In English)

Marchenko, A. V., Nasredinov, F. S., Kiselev, V. S., Seregin, P. P. (2018a) Analysis of the parameters of the Mössbauer spectra and the spectra of nuclear quadrupole resonance of the superconducting ceramic $YBa_2Cu_3O_7$. *Glass Physics and Chemistry*, 44 *(2)*, 92–99. https://doi.org/10.1134/S1087659618020116 (In English)

Marchenko, A. V., Nasredinov, F. S., Kiselev, V. S. et al. (2018b) Effective charges of atoms of HTSC $La_{2-x}Sr_xCuO_4$ ceramics determined from the analysis of the parameters of the nuclear quadrupole interaction. *Glass Physics and Chemistry*, 44 *(5)*, 412–417. https://doi.org/10.1134/S1087659618050115 (In English)

Masterov, V. F., Nasredinov, F. S., Seregin, P. P. (1995) Nuclear quadrupole interaction in high-temperature superconductors based on copper metal-oxides. *Physics of the Solid State*, 37, 1265–1292. (In English)

Mitsen, K., Ivanenko, O. (2007) The common origin of the pseudogap- and 60 K-phases in YBCO. *Physica C: Superconductivity*, 460–462 (2), 1094–1095. https://doi.org/10.1016/j.physc.2007.03.224 (In English)

Ohsugi, S. (1995) Doping dependence of the electric field gradiend at of La site in $La_{2-x}M_xCuO_4$ (M = Sr,Ba) La-NQR study. *Journal of the Physical Society of Japan*, 64 (10), 3656–3659. https://doi.org/10.1143/jpsj.64.3656 (In English)

Ohsugi, S., Kitaoka, Y., Ishida, K. et al. (1994) NMR study of magnetism and superconductivity in superconducting $La_{2-x}Sr_xCuO_4$. *Physica C: Superconductivity*, 235, 1633–1634. (In English)

Pennington, C. H., Durand, D. J., Slichter, C. P. (1989) Static and dynamic Cu NMR tensors of $YBa_2Cu_3O_{7-x}$. *Physical Review B*, 39 (4), 2902(R)–2905(R). https://doi.org/10.1103/PhysRevB.39.2902 (In English)

Schwarz, K., Ambrosch-Draxl, C., Blaha, P. (1990) Charge distribution and electric-field gradients in $YBa_2Cu_3O_{7-x}$. *Physical Review B*, 42 (4), 2051–2061. https://doi.org/10.1103/physrevb.42.2051 (In English)

Seregin, N. P., Masterov, V. F., Nasredinov, F. S. et al. (1992) Parameters of the electric field gradient tensor determined by ^{57}Co(^{57}Fe) and ^{67}Cu(^{67}Zn) emission Mossbauer spectroscopy for $La_{2-x}Sr_xCuO_4$ copper sites. *Superconductor Science and Technology*, 5 (11), 675–678. https://doi.org/10.1088/0953-2048/5/11/014 (In English)

Seregin, N. P., Marchenko, A. V., Seregin, P. P. (2015) *Emission Mössbauer spectroscopy. Electron defects and Bose-condensation in crystal lattices of high-temperature superconductors*. Saarbrücken: LAP Lambert Publ., 332 p. (In English)

Shimizu, T. (1993) On the electric Field Gradient at copper nuclei in oxides. *Journal of the Physical Society of Japan*, 62 (2), 772–778. https://doi.org/10.1143/JPSJ.62.772 (In English)

Shore, J., Yang, S., Haase, J. et al. (1992) Barium nuclear resonance spectroscopic study of $YBa_2Cu_3O_7$. *Physical Review B*, 46 (1), 595–598. https://doi.org/10.1103/physrevb.46.595 (In English)

Sun, J., Remsing, R. C., Zhang, Y. et al. (2016) Accurate first-principles structures and energies of diversely bonded systems from an efficient density functional. *Nature Chemistry*, 8, 831–836. https://doi.org/10.1038/nchem.2535 (In English)

Sun, J., Ruzsinszky, A., Perdew, J. P. (2015) Strongly constrained and appropriately normed semilocal density functional. *Physical Review Letters*, 115, article 036402. https://doi.org/10.1103/PhysRevLett.115.036402 (In English)

Takigawa, M., Hammel, P. C., Heffner, R. H. et al. (1989) ^{17}O NMR study of local spin susceptibility in aligned $YBa_2Cu_3O_7$ powder. *Physical Review Letters*, 63, 1865–1868. https://doi.org/10.1103/PhysRevLett.63.1865 (In English)

Tarascon, J. M., Greene, L. H., Mckinnon, W. R. et al. (1987) Superconductivity at 40 K in the oxygen-defect $La_{2-x}Sr_xCuO_{4-y}$. *Science*, 235 (4794), 1373–1376. https://doi.org/10.1126/science.235.4794.1373 (In English)

Terukov, E. I., Marchenko, A. V., Seregin, P. P. et al. (2018) Parameters of nuclear quadrupole interaction and spatial distribution of electronic defects in $YBa_2Cu_3O_7$ and $La_{2-x}Sr_xCuO_4$ lattices. *Physics of the Solid State*, 60 *(10)*, 1908–1915. https://doi.org/10.1134/S106378341810027X (In English)

Wells, A. F. (1984) *Structural inorganic chemistry*. Oxford: Clarendon Press, 1416 p. (In English)

Wortmann, G., Kolodziejczyk, A., Bergold, M. et al. (1989) Mossbauer studies of $YBa_2Cu_3O_{7-x}$ type high-Tc superconductors. *Hyperfine Interactions*, 50, 555–567. https://doi.org/10.1007/BF02407691 (In English)

Yu, J., Freeman, A. J., Podloucky, R. et al. (1991) Origin of electric-field gradients in high-temperature superconductors: $YBa_2Cu_3O_7$. *Physical Review B*, 43 (1), 532–541. https://doi.org/10.1103/PhysRevB.43.532 (In English)

Yvon, K., Francois, M. (1989) Crystal structure of high-T_c oxides. *Zeitschrift für Physik B*, 76. 413–444. https://doi.org/10.1007/bf01307892 (In English)

Summaries in Russian / Информация о статьях на русском языке

Физика конденсированного состояния

ИССЛЕДОВАНИЕ МОЛЕКУЛЯРНОЙ ПОДВИЖНОСТИ В КОМПОЗИТНЫХ ПЛЕНКАХ НА ОСНОВЕ ПОЛИЭТИЛЕНА

Гороховатский Юрий Андреевич, Волгина Елена Алексеевна, Иванова Анна Николаевна, Темнов Дмитрий Эдуардович

Аннотация

В работе методами термостимулированной деполяризации и дифференциальной сканирующей калориметрии исследовалась α-релаксация в композитных пленках на основе полиэтилена низкой плотности с частицами сажи. Показано, что совместное применение этих методов может быть использовано для определения количества релаксаторов, принимающих участие в релаксационных процессах полимера выше его температуры стеклования. Вычислены параметры и количество электрически активных дефектов в композитных пленках на основе полиэтилена с разным процентным содержанием технического углерода.

Ключевые слова: композитные пленки на основе полиэтилена, термоактивационная спектроскопия, дифференциальная сканирующая калориметрия, релаксация, электрически активные дефекты

Для цитирования: Gorokhovatskiy, Yu. A., Volgina, E. A., Ivanova, A. N., Temnov, D. E. (2022) Molecular mobility research in polyethylene composite films. *Physics of Complex Systems*, 3 (2), 55–59. https://www.doi.org/10.33910/2687-153X-2022-3-2-55-59. EDN EAWOSX.

ЭЛЕКТРОФИЗИЧЕСКИЕ СВОЙСТВА КОМПОЗИТНЫХ ПЛЕНОК НА ОСНОВЕ ХИТОЗАНА И ОДНОСТЕННЫХ УГЛЕРОДНЫХ НАНОТРУБОК

Камалов Алмаз Маратович, Кодолова-Чухонцева Вера Владимировна, Иванькова Елена Михайловна, Борисова Маргарита Эдуардовна, Юдин Владимир Евгеньевич

Аннотация

Разработаны и получены электропроводящие композитные пленки на основе хитозана и одностенных углеродных нанотрубок. С помощью метода сканирующей электронной микроскопии проведено исследование структуры композиционных пленок. Показано, что введение углеродных нанотрубок приводит к упорядочению структуры хитозана. При увеличении содержания нанотрубок от 0 до 3% происходит рост электропроводности от 10^{-11} до 10 См/м, изменение диэлектрической проницаемости от 5,5 до 26 на 1 кГц. Изучено влияние влаги на диэлектрические свойства композитных пленок.

Ключевые слова: хитозан, нанотрубки, электропроводность, диэлектрические свойства, порог перколяции

Для цитирования: Kamalov, A. M., Kodolova-Chukhontseva, V. V., Ivan'kova, E. M., Borisova, M. E., Yudin, V. E. (2022) Electrophysical properties of chitosan-based composite films filled with single-wall carbon nanotubes. *Physics of Complex Systems*, 3 (2), 60–65. https://www.doi.org/10.33910/2687-153X-2022-3-2-60-65. EDN HISZON.

Теоретическая физика

АНАЛИТИЧЕСКИЕ ЗАКОНОМЕРНОСТИ БЕЗИНВЕРСИОННОГО СВЕРХИЗЛУЧЕНИЯ

Горбачева Алиса Сергеевна, Рыжов Игорь Викторович

Аннотация

Теоретически исследовано сверхизлучение трехуровневых оптических систем с дублетом в основном состоянии (Λ-схема), помещенным в высококачественный резонатор. На поверхности многомерного тора без диссипативных потерь в условиях сверхизлучения без инверсии населенностей возникает гиперболический хаос и непредсказуемые динамические движения системы. Получены законы сохранения, позволяющие уменьшить размерность фазового пространства. Получен аналитический результат для частного случая вырожденного дублета.

Ключевые слова: сверхизлучение, сверхизлучение без инверсии, Λ-схема, уравнение Дюффинга

Для цитирования: Gorbacheva, A. S., Ryzhov, I. V. (2022) Analytical regularities of inversionless superradiance. *Physics of Complex Systems*, 3 (2), 66–74. https://www.doi.org/10.33910/2687-153X-2022-3-2-66-74. EDN KDLQJF.

ТЕРМОЭЛЕКТРОКИНЕТИЧЕСКИЕ ЯВЛЕНИЯ В КОНВЕКТИВНОЙ ЗОНЕ ПЛАЗМЫ СОЛНЦА И ЗВЕЗД

Грабов Владимир Минович, Зайцев Андрей Анатольевич, Кузнецов Денис Владимирович, Сидоров Александр Валентинович, Семенова Елена Юрьевна

Аннотация

Показано, что электромагнитные явления в зоне конвективной плазмы Солнца и звезд, локальное магнитное поле вблизи поверхности Солнца обусловлены не только механизмом магнитогидродинамического динамо, но и недавно обнаруженными и исследованными термоэлектрокинетическими явлениями в вязкой электропроводящей среде при наличии температурного градиента.

Ключевые слова: термоэлектрокинетические явления, вязкое электропроводящее вещество, плазма Солнца, конвективная зона Солнца, магнитное поле вблизи поверхности Солнца

Для цитирования: Grabov, V. M., Zaitsev, A. A., Kuznetsov, D. V., Sidorov, A. V., Semenova, E. Yu. (2022) Thermoelectrokinetic phenomena in the convective plasma zone of the Sun and stars. *Physics of Complex Systems*, 3 (2), 75–80. https://www.doi.org/10.33910/2687-153X-2022-3-2-75-80. EDN KSMTED.

НЕЛИНЕЙНОСТЬ ПРОСТРАНСТВА-ВРЕМЕНИ ВАЙДЬЯ И СИЛЫ В ЦЕНТРАЛЬНОЙ ГОЛОЙ СИНГУЛЯРНОСТИ

Вертоградов Виталий Дмитриевич

Аннотация

В данной работе мы рассматриваем нелинейное пространство-время Вайдья, т. е. случай, когда функция масс имеет нелинейный вид. Мы доказываем, что центральные голые сингулярности могут образоваться при значениях, но они будут гравитационно слабы. Также исследуется вопрос о силах в голой сингулярности и доказывается, что они могут быть конечными только в случае гравитационно слабой голой сингулярности. Рассмотрен вопрос о силе сингулярности. Мы доказываем, что сильная голая сингулярность может образоваться только в линейном случае или сингулярность может быть гравитационно сильной в случае образования черной дыры.

Ключевые слова: пространство-время Вайдья, голая сингулярность, сила сингулярности, силы инерции, геодезические, гравитационный коллапс

Для цитирования: Vertogradov, V. D. (2022) Non-linearity of Vaidya spacetime and forces in the central naked singularity. *Physics of Complex Systems*, 3 (2), 81–85. https://www.doi.org/10.33910/2687-153X-2022-3-2-81-85. EDN MWCGSM.

Физика полупроводников

ЭЛЕКТРОННЫЕ ДЕФЕКТЫ В РЕШЕТКАХ $YBa_2Cu_3O_7$ И $La_{2-x}Sr_xCuO_4$

Марченко Алла Валентиновна, Серегин Павел Павлович, Киселев Валентин Сергеевич

Аннотация

Используя данные эмиссионной мессбауэровской спектроскопии на изотопе ^{67}Zn и ядерного квадрупольного резонанса на изотопе ^{17}O, а также расчеты решеточного градиента электрического поля, определены эффективные заряды всех атомов кристаллических решеток сверхпроводящих металлоксидов меди $YBa_2Cu_3O_7$ и $La_{2-x}Sr_xCuO_4$. Эффективные заряды атомов металлов и большинства атомов кислорода соответствуют стандартным степеням их окисления (Y^{3+}, La^{3+}, Ba^{2+}, Sr^{2+}, Cu^{2+}и O^{2-}). Однако, атомы цепочечного кислорода (в $YBa_2Cu_3O_7$) и планарного кислорода (в $YBa_2Cu_3O_7$ и $La_{2-x}Sr_xCuO_4$) демонстрируют пониженный заряд, что объясняется локализацией в соответствующих подрешетках дырки.

Ключевые слова: Мессбауэровская спектроскопия, ядерный квадрупольный резонанс, тензор градиента электрического поля, заряды атомов, высокотемпературные сверхпроводники

Для цитирования: Marchenko, A. V., Seregin, P. P., Kiselev, V. S. (2022) Electronic defects in lattices of $YBa_2Cu_3O_7$ and $La_{2-x}Sr_xCuO_4$. *Physics of Complex Systems*, 3 (2), 86–99. https://www.doi.org/10.33910/2687-153X-2022-3-2-86-99. EDN NFNKXG.